

©2021. Licensed under the Creative Commons Attribution-NonCommercial-NoDerivatives 4.0 International <http://creativecommons.org/about/downloads>



This is the accepted version of this paper. The version of record is available at <https://doi.org/10.1016/j.compstruct.2021.114567>

# Quasi-static and low-velocity impact behavior of the bio-inspired hybrid Al/GFRP sandwich tube with hierarchical core: Experimental and Numerical Investigation

Amirreza Tarafdar<sup>a</sup>, Gholamhosein Liaghat<sup>a,b,\*</sup>, Hamed Ahmadi<sup>a</sup>, OmidRazmkhah<sup>c</sup>, SahandChitsaz Charandabi<sup>c</sup>, Moslem RezaeiFaraz<sup>a</sup>, EhsanPedram<sup>d</sup>

<sup>a</sup> Department of Mechanical Engineering, Tarbiat Modares University, Tehran, Iran.

<sup>b</sup> School of Mechanical & Aerospace Engineering, Kingston University, London, England, United Kingdom.

<sup>c</sup> Department of Mechanical Engineering, Coventry University, Coventry, UK.

<sup>d</sup> Department of Mechanical Engineering, Islamic Azad University, Takestan, Qazvin, Iran.

\*(corresponding author: [ghlia530@modares.ac.ir](mailto:ghlia530@modares.ac.ir))

## ABSTRACT

---

Sandwich tube structures bio-mimicking horsetail and human tendons offered significant improvement over traditional single and multi-cell tubular energy absorbers. The present research aims to investigate three manufactured hybrid multi-cell aluminum and GFRP sandwich tubes subjected to quasi-static and low-velocity axial compression. The crashworthiness characteristics and axial crushing failure mechanisms of sandwich tubes are discussed and compared with the quasi-static axial behavior of single Al and GFRP tubes. Further investigations, based on the validation of an FE model versus experimental results, using the commercial finite element code LS-DYNA, on the effects of material permutation and inner tubes diameter are perceived through the full-factorial approach of FE parametric study. The quasi-static results revealed that, packing the Al and GFRP tubes in the form of multi-cell sandwich tube generally improves the crushing patterns of individual hollow tubes. Moreover, the low-velocity response of the hybrid multi-cell sandwich tubes showed that the crushing response of the GFRP components despite AL ones depends significantly on the strain rate, where Al tubes undergo irregular diamond deformation. Eventually the results of bio-inspired hybrid multi-cell sandwich tubes indicate that incorporating more GFRP tubes provided an optimal crashworthy design and conduce to a broad range of applications within aerospace, transportation.

**Key words:** sandwich tube, multi-cell, energy absorber, low-velocity, bio-inspired, hybrid.

## 1. Introduction

The demand for energy absorbers is nowadays increasingly gained in aerospace [1], marine [2], chemical creations[3] and high-pressure containers [4], and the transportation sector[5]. Hence mechanical engineers are focusing on the construction of safe and reliable crashworthy productions which attenuate the damage to whatever is being transported. During a collision, energy-absorbing structures degrade most of the energy exerted against a vessel. In the design of such sensitive elements as the loading conditions, the geometry of the section and the type of material are the major considerations [6-10]. In recent decades, many scientists have considered the effect of these elements on the energy absorption behavior of axially crushed profiles experimentally, numerically, and analytically [11-18]. With regard to the geometry, studies have unanimously recognized that thin-walled circular sections show incomparably the best energy absorption behavior [3, 19-22], which is depends heavily on the type of material in the profile. In addition to metallic materials such as steel and aluminum, composites are also being used, thanks to their significant capability; they are light-weight, with high modulus, ductility, ease of construction, and even higher specific energy absorption than metals [23-27]. Metals by their ductility can absorb enough energy to dissipate the kinetic energy in the form of plastic deformation mechanisms, including concertina and diamond deformation patterns [28, 29]. In contrast, composite structures consume the energy in the form of stable and unstable crushing mechanisms through delamination, fiber breakage and matrix cracking [30-32]. Palvania [33] concluded that in addition to hybrid structures, sections with complex and special shapes showed more crushing and energy absorption properties than conventional sections did.

The current concern with crashworthiness design in response to the demand for robust, cost-effective, and efficient energy absorbers, has led to novel designing methods including the combination of different materials and complex geometries, the use of foam in hollow sections and of crimping in the walls of sections, etc. Nia and Parsapour[34] investigated the crashworthiness of different single-cell and multi-cell tube sections experimentally and numerically, and concluded that multi-cell tubes with internal ribs connected at the mid-walls of the external tubes are more efficient than tubes with internal ribs at the corners. The above investigations, suggest that multi-cell thin-walled tubes have remarkable capacity for energy absorption and exhibit suitable performance to satisfy today's concerns.

However, the design of thin-walled crashworthy structures with better energy absorption efficiency than that of traditional sections is still a challenge for designers. Thus, novel design inspired by biological structures seems a promising way to profit from their essential properties, which derive from their adaptation over billions of years to meet a range of harsh conditions [35]. The hierarchical body structures of bio-mimic creatures have provided unrivalled inspiration for scientists constructing energy-absorbing structures. Many bio-mimetic structures have been inspired by the cellular and multi-walled structure of bamboo [36], horsetail plant [37], beetles[37], human

vessels[35] and bones[38] and their results have shown improved energy absorption and other crashworthy parameters (see Figure 1). Due to the fabrication limitations of bionic structures, a variety of engineering materials have been employed to manufacture these bio-inspired energy absorbers, such as aluminum, polymers, and FRP composites. The study of bio-inspired hybrid metallic/composite structures has seldom been investigated. Hybridizing involves the use of two different materials in combination, benefiting from the unique properties of each in the widespread construction of energy absorbers. Designing specific hybrid energy absorbers could thus benefit from both the stable plastic deformation of metal and the low weight and high modulus of a composite [39-42]. Recent studies on hybrid energy absorbers, which have examined various parameters such as the diameter, thickness, and material type of the fibers under study [20, 43, 44], have focused on twisting fibers around metal tubes. For instance, Liu et al. [45] experimentally evaluated the energy absorption capacity of a bio-inspired bi-tubular energy absorber by embedding four star-shaped ribs with different configurations between inner and outer walls. Their results indicate that interaction between the ribs and tubes has a significant impact on the crashworthiness indicators. Recently, Liang Ying et al. [38] experimentally studied the quasi-static crushing behavior of bio-inspired hybrid multi-cell Al/CFRP hierarchical tubes. Their research outcomes showed that the capacity to absorb energy considerably improved by means of this hierarchy. Packing net CFRP with Al tubes enhanced the progressive folding collapse of the Al tubes and crashworthiness metrics. Of course, in addition to the use of several materials simultaneously in the construction of the energy absorbers, the cost of purchasing materials and also the ease of manufacturing method are two very important criteria that must be considered in relation to applying the structure. The specific energy absorption of glass fibers is much lower than that of carbon fiber reinforced epoxy and is therefore of interest to designers of crashworthy structures, since the crash elements can be made more robust and cost efficient [46].

In order to consider the above-mentioned criteria, this paper uses E/glass fibers and aluminum tubes as the base material from which to manufacture the conceptual design of an energy absorbing structure. Moreover, this is fabricated by a modified manual laying up method and the final specimens are finished by embedding the GFRP and metal tubes inside a tube by means of a hierarchical perspective. The objective of the present investigation is to evaluate the energy absorption capability of Al/GFRP bio-inspired hybrid multi-cell sandwich tubes with hierarchical cores. Quasi-static and low-velocity compression tests were carried out to evaluate the energy absorption characteristics of these tubes with three representative material permutations and the features were further compared to the quasi-static response of single Al and GFRP tubes. To understand further the effects of various material permutations and the diameter of the tubes on the energy absorption characteristics, numerical parametric studies through a full-factorial approach were conducted, based on the validation of the FE model versus the experimental crushing response. The optimal designs were reached by considering the load bearing capacity, crush load efficiency, specific energy absorption, and stroke efficiency.

Figure 1

## 2. Experimental procedure

### 2.1 Material characterization

This study aims to investigate the effect of a circular hybrid multi-cell using fiber glass composites and aluminum on the crashworthiness characteristics of tubular sandwich energy absorbers. To achieve this aim, it used composite tubes made of E/Glass fiber laminate and extruded aluminum alloy 6061-T6 because of their specific lightness and high SEA (specific energy absorption). The physio-mechanical properties of woven and uni-directional E-glass fiber sheets and aluminum alloy were obtained by performing ASTM standard tests and are summarized in Table 1. In addition, the density (2700 kg/m<sup>3</sup>), elastic modulus (70 GPa), Poisson's ratio (0.33) and ultimate stress of aluminum alloy were measured on the basis of the E-8M standard test results.

Table 1

### 2.2 Geometry and topology

The biological structures, with their intricate and diverse schemes, require intelligent modification and simplification. However, the engineered construction of bio-inspired structures has yet to optimize by coming closest design to a **biological structure**. In this study, the inspiration for the experimental specimens was the circular hierarchical structural patterns of the horsetail, bamboo, and human vessels and tendons. Three types of bio-inspired hybrid multi-cell sandwich tubes were manufactured by embedding the tubes between two internal and external tubes as core components. Each sample was composed of an 8-circular E/glass composite core of the same height (h). The thickness of the walls in both the internal and external Al tubes was designated to be constant at 1 mm for each type of hybrid multi-cell sandwich tube. Manufactured samples with the same dimension were coded in order to simplify the identification and comparison tests results. The specimens were labeled ACA, ACC, and CCC, in which the first and third letters represent the internal and external tube materials respectively, and the second letter introduces the core material. The letters A and C indicate the aluminum and composite components of the tube, respectively. For instance, as depicted in Figure 2, the code ACA indicates that the external and internal tubes were of aluminum whereas the core was composite. To strengthen the test results, three specimens of each type of hybrid sandwich tube were tested and the average value was reported.

Figure 2

### 2.3 Composite tube fabrication

Composite tubes were fabricated by using combinations of [0/90] woven and Uni-directional E/glass fiber sheets and ML 506 epoxy matrix in a roll-wrapping process. **The reason for choosing the combination of woven and circumferential UD fiber is that manufacturing the GFRP core tube is challenging due to the high flexural strength of UD glass fibers through 0- and 90-degree directions during wrapping around the mandrel. Thus, the final manufactured GFRP tube has weak inter-laminar adhesion, poor surface finishing, and low quality.**

Combining three inner woven layers with three outer UD fibers in the circumferential direction makes the manufacturing process much easier to obtain a suitable crushing response. This method is an improved version of the manual laying up method of placing GFRP over a Teflon mandrel. The novelty of this method is that it exerts mechanical pressure on the wrapped layers. Moreover, in order to remove the excess resin trapped during manufacturing between the Dacron fiber sheets, these sheets were overwrapped around the GFRP fibers to ensure that the finished surface of the tubes was smooth and clean. To avoid any imperfection or delamination, pressure was applied to each specimen by belts in every 10-centimeter segment installed on two thick waxed semi-polymer pipes. All the tubes were fabricated under the same conditions with a pre-designated number of layers: three woven fiber sheets were located in the inner layer and three UD fiber sheets were wrapped in the circumference. Subsequently, the samples were cured 24 hours and then left for the post-cure process at room temperature for one week in order to become strong enough. The physical purpose of this In the present study, six samples were manufactured for each type of hybrid multi-cell sandwich tube to test their axial quasi-static and low-velocity crushing behavior. Figure 3 shows the final assembly of tube fabrication; this process was also used in manufacturing the external and internal composite tubes.

## 2.4 Test procedure

### 2.4.1 Quasi-Static test

The samples were quasi-static compressive axially loaded using a Universal Testing Machine (UTM) of 300 kN load capacity. The UTM has two parallel jaws; the lower is fixed and the upper is movable. The test was displacement controlled and the compressive axial loading rate was set to 5 mm/min. The diameter of the sample was large enough to ensure no sliding or slipping during the experiment. A 100 kN load-cell was used to record accurate load-displacement data. The axial crushing load-displacement curves were obtained and the absorbed energy (EA) of the sandwich tubes was calculated by integrating the area under the load-displacement curve. Crashworthiness indicators including Mean Crushing Load (MCL), Peak Crushing Load (PCL), Stroke Efficiency (Ste), Crush Load Efficiency (CLE), Specific Energy Absorption (SEA), Axial Elastic Stiffness (AES) were calculated and compared on the basis of the load-displacement profiles

### 2.4.2 Low-Velocity Impact test

Axial low velocity impact crushing tests were conducted using a drop hammer testing system in order to determine the energy absorption capacity of the sandwich tubes. Figure 4 shows the 44.90 kg carriage consisting of a circular rigid platen and an acceleration sensor lifted by a rigid magnetic plate connected to a servo-hydraulic motor. The accelerometer sensor was mounted on a moving carriage which slides up and down the guide rails at a rate of 96 KHz to measure the acceleration-time by a data acquisition system. After filtering the recorded data through a CFC 500 filter to remove signal noises, the displacement was measured by integrating the acceleration data twice and, in order to calculate the load, the filtered acceleration data was multiplied by the carriage mass.

In addition, during the impact tests, a high-speed camera with a rate of 1000 frame/s was used to capture the specimen crush deformation.

Figure 3

Figure 4

### 3. Numerical

#### 3.1 Numerical strategy

In order to learn more about the structural performance of the hybrid sandwich tubes, a numerical model was developed through an explicit nonlinear finite element code LS-DYNA in a double precision mode. The numerical strategy was based on modeling every component individually, to accurately predict the crushing behavior of the sandwich tubes. In the first stage, the generation of geometry was accomplished corresponding to the quasi-static axial compression experimental results for the composite and aluminum tubes.

#### 3.2 Finite element model

There are two ways to simulate the geometry of a composite tube: by multi- or single-layer simulation. Multi-layer strategy can predict the failure mechanisms, including central crack growth and inter-laminar delamination as well as peak and mean loads. Although failure mechanisms are not observed clearly in single-layer configuration, load-displacement curves can be predicted precisely within a short computational time. According to experimental observations, the delamination and central crack generation in composite tubes are initiated at the adjacent woven and UD layers. To verify this, a combination of single- and multi-layer approaches was adopted and woven and UD fibers were modeled in two separate shells. Two Belytschko-Tsay four-node shell elements were established, corresponding to the three woven and three circumferential UD layers. The same type of shell element also was used for the aluminum tubes. According to the dimensions of the tubes presented in Figure 2, the middle surface of the tubes was denoted the reference surface of each shell element. As illustrated in Figure 5, the equivalent diameter of fiber sheets and internal and external aluminum tubes were considered in light of the optimal thickness configuration. According to the number of woven and UD layers, 3 through thickness integration points were considered for each shell element, but only 5 integration points were applied for the aluminum tubes. To capture the actual boundary conditions, no constraints were laid on the tubes. Thus, both ends of the tubes were free and subjected to quasi-static axial compression by a displacement-controlled option named \*BOUNDARY\_PRESCRIBED\_MOTION-RIGID assigned to the upper rigid platen. The upper movable platen was translated in the vertical direction only and the lower rigid platen was completely constrained. To ensure that quasi-static conditions were being simulated, the kinetic to internal energy ratio had to be less than 5% [20, 47]. Figure 6 represents the ratio of kinetic to internal energy of the simulated tubes, in this case less than 2% except within a small range when the crushing began.

To find the mesh independency for the peak and mean load of each part, a mesh study was conducted by reducing the size of the element from 4 mm to 0.8 mm. The convergence obtained on a 1 mm element size led to

the most accurate numerical results. Therefore, the composite, external and internal aluminum tubes were determined to consist of 10710, 22860, 9630 number of elements respectively.

Figure 5

Figure 6

### 3.3 Material models

#### 3.3.1 Aluminum

The material model \*MAT\_MODIFIED\_PIECEWISE\_LINEAR\_PLASTICITY (MAT 123) is a functionally material model that was used to capture the elastic-plastic behavior of Aluminum 6061-T6. The advantage of this material model is that it supports an arbitrary stress versus strain curve as well as being dependent on an arbitrary strain rate. Moreover, this model benefited from enhanced failure criteria, based mainly on effective plastic strain and the major principal in-plane strain components [48]. The plasticity behavior of Aluminum may be formulated as follows:

$$\sigma_y = \beta[\sigma_0 + f_h(\varepsilon_{eff}^p)] \quad (1)$$

where  $\beta$  is Cowper-Symonds strain rate coefficient,  $\sigma_0$  defines static yield stress;

$$\beta = 1 + \left(\frac{\dot{\varepsilon}}{C}\right)^{1/P} \quad (2)$$

which C and P are corresponded to Cowper-Symonds coefficients. Alongside,

$$f_h(\varepsilon_{eff}^p) = E_p(\varepsilon_{eff}^p) \longrightarrow \text{linear hardening function} \quad (3)$$

$E_p$  = plastic hardening modulus

$\varepsilon_{eff}^p$  = effective plastic strain

The strain rates in the range of  $[10^{-4}- 10^3]$  (1/s) have no significant effects on the plastic behavior of aluminum alloy. Many researchers have indicated that aluminum alloy is insensitive to strain-rate effects in the  $10^{-4}-10^3$  range [28, 29]. Therefore, no strain hardening coefficients have been defined for aluminum alloy. It is worth noting that two distinct approaches are available to define the failure strain of aluminum. Although the failure strain can be calculated through the damage mechanism models of Peschmann and Rice-Tracey & Crockcroft-Latham (RTCL), while the yield stress is defined, the failure strain can be determined by considering the dynamic yield stress [48].

#### 3.3.2 Glass/Epoxy composite

According to many studies [24, 49, 50], \*MAT\_ENHANCED\_COMPOSITE\_DAMAGE (Mat\_54) is an efficacious material model for predicting the crush behavior of composite tubes. This damage model can be

validated for thin wall shell elements only and its failure criteria are suggested by Chang-Chang[48]. Specifying an appropriate local material axis and constitutive constants enables the users to define arbitrary orthotropic properties. The constitutive equations are used to calculate the strains in terms of stresses within the plane stress state. These equations, which change through the thickness of the shell, are formulated as follows:

$$\begin{aligned}\varepsilon_{11} &= \frac{1}{E_1}(\sigma_{11} - \nu_{12}\sigma_{22}) \\ \varepsilon_{22} &= \frac{1}{E_2}(\sigma_{22} - \nu_{21}\sigma_{11}) \\ 2\varepsilon_{12} &= \frac{1}{G_{12}}\tau_{12} + \alpha\tau_{12}^3\end{aligned}\tag{4}$$

The shear stress and strain relationship in the plane stress condition is defined as  $\alpha$  and the in-plane shear modulus is specified as  $G_{12}$ .

The failure criteria are based on both tensile and compressive fiber failure and on the matrix failure mode. Hence the relationship between the tensile fiber failure with stiffness degradation that meets the failure criteria is given as follows:

$$\varepsilon_f^2 = \left(\frac{\sigma_{11}}{x_t}\right)^2 + \beta\left(\frac{\sigma_{12}}{s_s}\right)^2 - 1 \geq 0 \quad \text{where } \sigma_{11} > 0 \Rightarrow \varepsilon_f^2 \geq 0 \rightarrow \text{failed}\tag{5}$$

When the failure criteria are met, the lamina degradation stiffness applies and all the elastic constants including  $E_1, E_2, G_{12}, \nu_{12}, \nu_{21}$  are reduced to zero.

The relationship between the compressive fiber failure with stiffness degradation and the failure criteria is given as follows:

$$\varepsilon_c^2 = \left(\frac{\sigma_{11}}{x_c}\right)^2 - 1 \geq 0 \quad \text{where } \sigma_{11} < 0 \Rightarrow \varepsilon_c^2 \geq 0 \rightarrow \text{failed}\tag{6}$$

If the element layer fails, the elastic constants  $E_1, \nu_{12}, \nu_{21}$  are degraded to zero.

The failure criterion for the tensile matrix mode is:

$$\varepsilon_m^2 = \left(\frac{\sigma_{22}}{y_t}\right)^2 + \left(\frac{\sigma_{12}}{s_c}\right)^2 - 1 \geq 0 \quad \text{where } \sigma_{22} > 0 \Rightarrow \varepsilon_m^2 \geq 0 \rightarrow \text{failed}\tag{7}$$

Once the failure criterion formulation is satisfied,  $E_2, G_{12}, \nu_{21}$  are set to zero.

The failure criterion for the compressive matrix mode is:

$$\varepsilon_d^2 = \left(\frac{\sigma_{22}}{2s_c}\right)^2 + \left[\left(\frac{Y_c}{2s_c}\right)^2 - 1\right] \frac{\sigma_{22}}{Y_c} + \left(\frac{\sigma_{12}}{s_c}\right)^2 - 1 \geq 0 \text{ where } \sigma_{22} < 0 \Rightarrow \varepsilon_d^2 \geq 0 \rightarrow \text{failed} \quad (8)$$

After the lamina failure because of the compressive matrix mode, the elastic constants are set to zero, i.e.  $E_2$ ,

$$G_{12}, \nu_{12}, \nu_{21} = 0$$

Indices 1 and 2 specify the two principal directions of the material, the fiber direction and the transverse direction for both woven and UD fiber sheets, respectively.  $\sigma$  indicates the stress developed during deformation. The material model behaves in a linear elastic way in tension, compression, and shear until the developed stresses of the element reach their current yield strengths. Element erosion was applied while the strains increased up to the maximum failure point when the stresses were kept constant. The other material parameters in Equations (4)-(8) are defined in Table 1. Further parameters of the material model are characterized in Table 3.  $\beta$  was a weighting factor for the shear term in tensile fiber failure, which was set to 1 if  $\beta$  was a weighting factor. The Hashin failure criteria were chosen for the failure mode and if  $\beta$  had been equal to 0, the maximum stress criteria have been treated as failure criteria. After much trial and error, the numerical and experimental results came close to agreement when BETA was set as 1. The stiffness degradation caused unusual distortion of the element, requiring excessive hourglass energy and more computational run time. Thus, it appears that element erosion needs to be adopted by the DFAILT, DFAILC and DFAILM options. In addition, some elements deformed and became greatly distorted, causing negative Jacobian and stopping the program during analysis. This activated the NFAIL1 and NFAIL4 and DELFR element removal tools in \*CONTROL\_SHELL. All the failure parameters are defined in Table 2, below.

**Table 2**

### 3.4 Contact definition

In this study, to achieve more accurate numerical results, three crucial types of contact algorithm were defined. \*CONTACT\_AUTOMATIC\_SINGLE\_SURFACE was used for each shell element to prevent self-penetration. \*CONTACT\_AUTOMATIC\_SURFACE\_TO\_SURFACE was adopted to simulate the interactions between the tube and the rigid platen. Using Segment-based soft option 2 in this type of contact ensures that the shell elements do not penetrate to the solid elements of a rigid platen. \*CONTACT\_AUTOMATIC\_SURFACE\_TO\_SURFACE\_TIEBREAK models the interaction and bonding between two adjacent composite layers. Thus, the inter-laminar delamination can be featured. The debonding of nodes which have initially been tied together occurs when the failure criterion is satisfied, as below:

$$\left(\frac{|\sigma_n|}{NFLS}\right)^2 + \left(\frac{|\sigma_s|}{SFLS}\right)^2 \geq 1 \quad (9)$$

NFLS and SFLS introduce interfacial normal and shear failure strengths while  $\sigma_n$  and  $\sigma_s$  are the normal and shear stresses applied on the interface surface during the crushing process. Satisfying Equation (9) leads to

reducing the interfacial stress to zero and detaching the two tied nodes. Then this contact algorithm acts as a \*CONTACT\_AUTOMATIC\_SURFACE\_TO\_SURFACE. In this study, the normal and shear strengths were chosen to be 155 and 90 MPa respectively, figures obtained from the adhesive manufacturer's datasheet[51].

### 3.5 Modeling hybrid multi-cell tubes

The sandwich tube was modeled by assembling the individual simulated parts according to the current literature (see Figure 7). Symmetric geometry and boundary conditions make it possible to use couple modeling in the finite element software. Thus, modeling a half or a quarter of the sample considerably reduces the computing time[51]. To discount the effect of size reduction, symmetric boundary conditions were applied. It is worth mentioning that modeling the quarter of the specimens predicts the failure mechanisms and the load-displacement curves well, but to achieve the accurate failure mechanisms, a complete model was simulated to illustrate the suitable failure mechanisms meanwhile the load-displacement curves of two type of models corresponding to same specimen matched well. The top end of the sandwich tube was subjected to quasi-static axial compression by a rigid platen and all the degrees of freedom of the lower platen were fixed. The only difference between the model of the sandwich tube and individual tubes was the defining of additional \*CONTACT\_AUTOMATIC\_SURFACE\_TO\_SURFACE for non-adjacent shell elements. Figure 8 represents the kinetic to internal energy ratios of the quasi-static simulations, which were under 5%. Low velocity impact tests were simulated by rectifying the quasi-static model of sandwich tube where the initial velocity was set to the upper rigid platen instead of \*BOUNDARY\_PRESCRIBED\_MOTION-RIGID. In addition, the strain rate effects on Al and GFRP tubes is discussed in section 4.3.

Figure 7

Figure 8

## 4. Results and discussion

### 4.1 Quasi-static axial compression of single hollow tubes

The axial collapse behavior of single Al and GFRP tubes should primarily be evaluated to identify the deformation modes of the manufactured bionic hybrid multi-cell sandwich tubes. In this regard, the quasi-static compression response of the GFRP tube was analyzed experimentally and numerically. The geometric characteristics of a metal circular tube such as the ratio of its height to its diameter (H/D) and the ratio of its diameter to its thickness (D/T) affect the axial plastic deformation mode [52]. For this reason in the present study, net AL tubes 90 mm high and 1 mm thick but with different diameters were tested axially under compression loading to investigate their collapse modes. Both Al tubes deformed within the plastic formation of stable progressive folding, exhibiting a non-axisymmetric diamond mode with the same number of circumferential corners (Figure 9(a)-(b)). As can be seen from Figure 9, internal and external tubes present different folding patterns for the H/D variation and the D/T variation. The symmetrical folding formation of the

internal tube could be observed where the non-symmetrical converse folding for the external tube occurred, generating folds of different shapes with varying angles. According to the simulated axially crushed Al tubes represented in Figure 9 (a2)-(b2), the numerical prediction of deformation modes was in reasonable agreement with the experiments. As shown in Figure 10 (a1)-(b1), the numerical and the experimental load-displacement curves followed a fairly similar trend. The curve was determined either by elastic deformation or plastic folding. The elastic stage ended by reaching the load to PCL, followed by a sharp drop to MCL. Fluctuations in the diagram correspond to the progressive plastic folding. During the steadily progressive folding of the internal Al, the differences of MCL and PCL between the numerical analysis and the experiment were 0.210 kN (3.24%) and 0.639 kN (5.71%), respectively. The calculated errors corresponding to the MCL and PCL of the external Al were 0.53 kN (3.4%) and 0.80 kN (1.97%). It should be noted that the load-displacement curve of the external Al did not fluctuate regularly about an MCL and deformed irregularly, which may have corresponded to manufacturing errors and the ratio of h/d and d/t. The Stes of both AL tubes were above 60% but the CLEs of the internal and external tubes were 57.98 and 36.58 %, respectively. From Figure 10 (a2)-(b2), it appears that the EA and SEA increase steadily and almost linearly, except for a rapid increase in the elastic deformation stage. The differences of EA and SEA between the numerical and experimental internal Al tubes were 9.89 J (2.54%) and 4.12 J/gr (2.52%) respectively, and for the external ones were 34.54 J (3.53%) and 1.03 J/gr (6.65%), respectively. The slopes of the EA and SEA diagrams for the internal Al tube were 6.48 J/mm and 0.27 J/(gr.mm) and for the external Al tube were calculated as 15.19 J/mm and 0.24 J/(gr.mm), respectively.

Figure 9

The energy absorption capability in tubular energy absorbers depends on the failure mechanisms. Notwithstanding the dissipation of energy in the metal tubes through plastic folding, the composite tubes absorb energy in two distinct processes: catastrophic failure and progressive crushing. The tubular composite energy absorbers have to be efficiently designed to avoid catastrophic failure. The reason is that increasing the crush load too quickly, followed by a sharp drop to a low crush load, mid-plane circumferential fiber breakage and structure instabilities results in less EA and load bearing capacity and a lower Ste. In contrast, a more suitable progressive crushing mode is achieved by increasing the crush load to an initial peak and then reducing the crushing load to a steady state. One of the main differences between the tested GFRP and the Al tubes was the value of the load drop after PCL. In Al tubes, rather than GFRP tubes, the load after PCL declines to a valley and fluctuates at a lower MCL. Thus, the amount of CLE for a composite tube is much higher than for an Al tube. This behavior is bound up with the progressive crushing failure of composite tubes which absorbs energy through brittle fracture failure and friction, unlike the plastic deformation of Al tubes. Brittle fracture failure is composed of a splaying mode (laminar bending) and a transverse shearing mode. In the splaying mode, the propagation of longitudinal cracks through radial direction induces the splaying of material in a petal-like shape.

At the same time, the inter-laminar crack propagation which was accompanied by debris wedges when the crushing began led to the formation of internal and external fronds. The friction between the layers during the bending of the lamina, and the friction between the fronds and the loading platen were also dissipation mechanisms of energy absorption. The transverse shearing mode is characterized by a wedge-shape laminate cross-section. As the platen moves down, the contributions of propagated inter-laminar and longitudinal cracks result in the fracture of laminar bundles. These cracks, as observed in the experimentation, were shorter than the cracks generated in the splaying mode. The predicted damage mechanisms of FEM were very similar to those observed in the experiment (see Figure 11) and the load-displacement, EA and SEA curves of FE analysis were matched well, as illustrated in Figure 12.

Figure 10

The GFRP tube was crushed progressively with the longitudinal inter-laminar crack propagation when the crushing began. As the load reaches the PCF, woven fibers tend to fail in a catastrophic failure mode because the fibers in the warp and weft directions have equal strength. However, circumferential UD fibers act as belts around the woven fibers and prevent the inner woven fiber from bending outwards. Farely et al. [53] stated that most of the circumferential stiffness of UD fibers hastens inter-laminar crack propagation. Thus, the inter-laminar crack propagation, lamina bending and longitudinal crack propagation in the radial direction cause the crush load to rise to a maximum peak load of 28 mm displacement. However, in the experiment a sudden sharp load drop occurred with a 24 mm displacement due to the transverse shearing mode related to the micro fracture of the laminar bundles. Subsequently, the propagation of intra-laminar cracks ended by shearing away the edges of the laminar bundle and fiber breakage. From Figure 12 (a) for GFRP tube, it is evident that the linear trend of the load-displacement curve of FE analysis and experiment was well adapted and the variation errors of PCL and MCL were 0.12 kN (6%) and 0.08 kN (5.10%), respectively, which is an acceptable result. The Ste of the GFRP tube was equal to 82.5%. The difference of CLE between the FE analysis and the experimental result was negligible and the value of CLE was 76.78%. Comparison between the Al and GFRP tubes revealed that the performance of the GFRP tube was considerably higher in terms of CLE and Ste. As can be seen from Figure 12 (b), the trend of EA and SEA of the GFRP tube in the experimental and FEM increased linearly by increasing the crushing length. The variation between the EA and SEA in the FEM and experiment was 6.06%. The experimental increment ratios of EA and SEA were about 1.37 J/mm and 0.13 J/(gr.mm), respectively. Compared to the growth ratio of the Al tubes, the increasing rates of EA and SEA in the composite tubes were very low, especially in the elastic stage of the crushing process, as shown in Figure 12 (b).

Figure 11

According to the irregular plastic deformation mode and the rather poor performance of the external Al tube compared to the internal Al and GFRP tubes, the hybridization of various sizes of GFRP and Al tubes has excellent potential to improve the crashworthiness efficiency and cost-performance of a novel bio-inspired sandwich tube.

Figure 12

#### 4.2 Quasi-static axial crushing of bio-inspired hybrid sandwich tubes

The crushing response and crashworthiness characteristics of Al and GFRP tubes were analyzed and discussed specifically in the previous section. Although both Al tubes deformed in the diamond mode, the external, but not the internal Al tube showed irregular deformation and an unsuitable crush response. In addition, the GFRP core was progressively crushed and displayed the expected crashworthiness indicators. The FE models were able to predict reasonably the characteristics of collapse deformation and crashworthiness corresponding to single hollow tubes. The following section deals with the energy absorption characteristics and collapse behavior of the manufactured bio-inspired hybrid multi-cell sandwich tubes.

Figure 13 illustrates the typical load-displacement curve of an ACA sandwich tube where the PCL is equal to 70.60 kN in the pre-crushing stage, notably higher than the PCL of a single hollow tube. Moreover, the calculated value of MCL was 38.80 kN. This value is greater than that of the MCL of single Al and GFRP tubes which had been calculated equal to 15.19, 6.48, and 1.37 kN, respectively. Thus, the ACA sandwich tube possesses higher load capacity and energy absorption potential than single hollow tubes do. The ratio of the load increasing relative to 0-0.36 mm displacement (AES) is equal to 195.08 kN/mm, corresponding to the pre-crushing stage. It can be seen that the interaction of Al and GFRP tubes considerably increases the load and energy capacity of the ACA sandwich tubes and this phenomenon leads to a more stable crushing displacement of the structure. After reaching the due load to the PCL in a 0.36 mm displacement, the ACA sandwich tube was crushed in a steadily progressive manner. As presented in Figure 14 (a1, a2), it can be calculated that integrating the Al and GFRP tubes led to a mixed-plastic deformation mode of the external Al tube, unlike the irregular diamond deformation mode of a single external Al tube. The Ste of the ACA sandwich tube was 52% compared to the higher Ste of the individual components (external and internal Al were above 60%, GFRP core was 82.5%). In contrast, the CLE value of ACA sandwich tube was 55.24%, which denotes a considerable improvement compared to the CLE of the external Al tube (36.58%). The EA diagram of the ACA multi-cell sandwich tube presented in Figure 13 reveals that packing single Al and GFRP tubes considerably promotes the EA – upto 1805.85 J – which is 1.83 times, 4.64 times and 17.61 times that of the single hollow tubes. Although the EA curve followed a linear trend in its post-crush progressive folding, the growth ratio of EA of the ACA in the elastic stage was lower than that of the single Al tubes and very much higher than that of the GFRP tube.

From the load displacement and energy absorption curves of the FE analysis corresponding to the ACA hybrid multi-cell sandwich tubes plotted in Figure 13, it is clear that a logical trend, especially in the elastic stage, can be observed in the experimental curves. The calculated crashworthiness parameters are tabulated in Table 3. The maximum error between the numerical and experimental values was 2.7% which corresponds to the mean crushing load. As is evident from Table 3, the numerical analysis results matched the experimental crashworthiness evaluation remarkably well.

Figure 13

Table 3

From the snapshot of the ACA hybrid multi-cell sandwich tube presented in Figure 14 (b), the dominant failure mechanisms of GFRP tubes were inter-laminar delamination and the transverse, and longitudinal fiber breakage. The progressive diamond folding of the Al tubes, especially the tendency of the external Al tube to deform in an irregular diamond mode, imposes a greater perpendicular load on the GFRP tubes through radial direction, and leads to internal progressive crushing and normal directional breaking of the GFRP core in the folding spots. In other words, the out-of-plane resistance to shrinkage of the woven layers in cooperation with the UD layers against a radial compressive load plus the load applied by the internal and external Al tubes, resulted in an MCL increment of the ACA sandwich tube in comparison with single Al and GFRP tubes and the improved plastic folding of the external Al tube.

Figure 14

Figure 14 (c) presents the collapsing pattern of FE analysis which agrees closely with the experimental deformation illustrated in Figure 14 (b). The FEA showed the transversal and circumferential fiber breakage and inter-laminar delamination well. But the element deletion option defined for the GFRP tubes prevented some internal fronds from being observed accurately. In contrast, the plastic deformation of the Al tubes was displayed accurately corresponding to a mixed deformation mode of the external Al tube and the regular diamond mode of the internal tube with six lobes. The material model obtained for Al tubes was able to analyze the crack propagation corresponding to the external Al tube.

Subsequently, the axial quasi-static response of the ACC bio-inspired hybrid multi-cell sandwich tube was investigated. The typical crush load-displacement and EA curves of ACC multi-cell sandwich tube are plotted in Figure 15. The ultimate end-crushing displacement was measured as 56.6 mm, corresponding to be roughly 62.88 % of the total height of the ACC sandwich tube, indicating the enhancement of  $St_e$  beyond the ACA multi-cell tube. According to the pre-crushing stage in Figure 15, the axial elastic stiffness of the ACC sandwich tube is computed as 11.54 kN/mm, denoting a 94.08% decrement in AES below that of the ACA. Increasing the load up to 39.15 kN of the PCL was followed by steady fluctuation of the crushing load, where the MCL was

calculated as 23.69 kN in the post-crush stage; this was higher than the 15.19 kN of MCL of the external net Al tube. It is worth mentioning that the effect of the internal and core GFRP tubes on the entire sandwich tube caused numerous fluctuations of the crushing load. The CLE of this type of sandwich tube is 60.51%, compared to the lower CLE of the ACA; moreover, the comparison of Ste between ACC and ACA denotes that the crushing integrity of the ACC sandwich tube is much more suitable than that of the ACA sandwich tube. The energy absorption curve of the ACC increased linearly up to 1341.05 J, except for a rapid increase in the elastic stage. The growth ratio of EA in the elastic stage corresponding to the ACC sandwich tube was 16.4 J/mm, compared to the ACA energy absorption growth ratio, which equalled 66.86 J/mm. Comparing the increment ratio of EA in the single Al and GFRP tubes presented in Figures 10 and 12, it can be concluded that the diminution in comparison with ACA specimen of the EA growth ratio of the ACC sandwich tube is due to replacing the GFRP internal tube instead of the Al tube. The load-displacement and EA curves of the FE analysis of the ACC hybrid multi-cell sandwich tube are comparatively presented in Figure 15. A rational trend is evident and the determined crush indicators in Table 4 also endorses the verification of the FEM results with negligible errors.

Figure 15

**Table 4**

The crushing process and failure mechanisms of the ACC hybrid multi-cell sandwich tube are illustrated in Figure 16. In the initial crushing process shown in Figure 16 (a1), the external Al tube started to fold from the two ends of the tube followed by concertina plastic deformation. By contrast, the number of corners of diamond deformation occurring in the middle of the crushing height observed in Figure 16 (a3 and a4) changed from 3 to 4. According to Figure 16 (b), the GFRP tubes crushed progressively in the axial direction in comparison with that of the ACA sandwich tube. From Figure 16 (b1), it can be seen that all the failure mechanisms of GFRP tubes are combinations of inter-laminar delamination and fiber breakage. Due to the substitution of the internal Al tube with the GFRP tube, the perpendicular load applied between each component of the ACC sandwich tube, rather than those of the ACA sandwich tube, was reduced, which led to lower normal directional breaking of GFRP tubes. The interactions between the internal and the core GFRP tubes induced internal fronds to form. In doing so, the interaction between the Al and GFRP tubes accompanied by the accumulation of the crushed debris of the GFRP tubes, translated the folding pattern of the external Al tube into the concertina mode, unlike the external Al diamond mode in the ACA sandwich tube, as presented in Figure 16(b2).

In addition, Figure 16 (c) illustrates the predicted failure morphology of the ACC hybrid multi-cell sandwich tube. Generally, the numerical results matched the experiments closely, especially in predicting the damage modes of the GFRP tubes and external Al tubes. However, in the erosion of the elements corresponds to the

GFRP tubes, the internal fronds were eroded in the descent of the upper platen. It is worth mentioning that FE analysis exhibited the onset of cracks in the external Al tube in the ACA sandwich (Figure 14 (b and c)) whereas no cracks were observed in the external Al tube in ACC. This phenomenon authenticated the accuracy of the FE model with regard to the multi-cell sandwich tube.

Figure16

In the last part of the quasi-static tests, the axial compression behavior of CCC hybrid multi-cell sandwich tube was investigated. The load-displacement and energy absorption of the CCC sandwich tube are depicted in Figure 17. From the diagram it seems that the first PCL occurred in 22.20 kN, followed by regular oscillation around 19.49 kN of the MCL. The calculated AES of the CCC sandwich tube was equal to 4.86 kN/mm, which showed a reduction of 97.50% and 57.88% below that of the ACA and ACC sandwich tubes, respectively. The reason for the reduced AES is related to the relative strength of the composite compared to that of the Al in the elastic stage. The contribution of more GFRP tubes induced lower axial elastic stiffness of the structure, resulting in lower AES values. The ultimate crushing displacement was determined as 60.41 mm. Thus, the Ste of the CCC was equal to 67.12%, indicating the improvement of Ste beyond that of ACA (52%) and of ACC (62.7%). Moreover, the CLE of the CCC sandwich tube was 86.19% which increased considerably beyond that of the ACA (55.24%) and ACC (60.51%) sandwich tubes, indicating that this type of material permutation shows stable progressive failure and integrity in crushing. The EA of the CCC sandwich tube followed a linear trend up to 1169.06 J and, according to the above EA growth ratio of a single Al and especially the GFRP tubes in the elastic stage, the growth ratio of CCC sandwich tube declined to 10.63 J/mm below that of the ACA and the ACC sandwich tubes.

The FE crushing response of the CCC multi-cell sandwich tube is presented in Figure 17, showing that the predicted load-displacement and EA of the numerical analysis correlate well with the experimental response. The crashworthiness parameters corresponding to CCC sandwich tubes versus the experimental results are compared in Table 5.

Figure 17

**Table 5**

The crushing morphology snapshots of the CCC multi-cell sandwich tube in Figure 18 reveal that the crushing modes of the GFRP tubes are very intricate and consist of a combination of intra-laminar fiber breakage, fracture of the laminar bundles, circumferential fiber fracture, shear fiber fracture and inter-laminar delamination. In the early stage of crushing history observed in Figure 17 (a1 and a2), due to the h/d and d/t ratios of the external tube, the perpendicular interactions of the external and core tubes as well as the initial local buckles of the inner tubes. Circumferential fiber breaking begins at the bottom of the tube followed by a progressive crushing of the

external GFRP tube (Figure 18 (a3-a6)). As the crushing process continued, the accumulation of debris and forming fronds internally within the inner GFRP tubes propagated the shear cracking at the upper end of the external tube corresponding to the final stage of the crushing process. It can be observed from Figure 18 (b1 and b2) that the external GFRP tube absorbs energy through laminar bundle fractures, intra-laminar fiber breakage, the propagation of shear, and circumferential and longitudinal cracks. From the top view of the sandwich tube, it seems that the inner GFRP tubes are crushed inwards, except at first, when small external fronds are formed. Figure 18 (b3) apparently illustrates inter-laminar delamination and intra-laminar fiber breakage of the internal tube. The FEA of the crushing behavior of the CCC sandwich tubes versus experimental crushed morphologies was validated, as presented in Figure 18 (c). The FEM clearly predicted the failure mechanisms including fracture of the laminar bundles, shear, and circumferential cracks. As noted above, due to the erosion of the failed elements, some small differences observed in the FE crushed specimen and experiment corresponded to the fronds which formed.

Figure 18

The SEA values of the manufactured multi-cell sandwich tubes are very close to each other, where the calculated SEA of the numerical approach showed good agreement with the experiment (see Figure 19). Although the percentage of reduced EA in the CCC specimens compared to the ACA specimens is 35.36%, the SEA increased by 15.28, but replacing the internal Al tube in the ACA sandwich tube with GFRP made no significant improvement in SEA except that the plastic folder of the external Al tube had increased the number of concertina folds. In summary, the evaluation of the results indicates that the ACA sandwich tube had higher PCL, MCL, and EA than the ACC and CCC sandwich tubes had. In contrast, the CCC sandwich tube showed the best SEA, CLE, and Ste compared to either the ACC or the ACA. By comparing the axial elastic stiffness of multi-cell sandwich tubes, it can be concluded that the external Al tube in ACA can greatly increase the AES of the structure in comparison with the ACC and CCC (the AES of ACA, ACC, and CCC are 195.08, 11.54, and 4.86 kN/mm, respectively). In general, in the cases demanding more load capacity and EA along side together with limited elastic stiffness, the ACA sandwich tube can be more effective. Meanwhile, demands for cost-effective and light-weight structures with higher SEA, Ste, CLE and less elastic stiffness requires the CCC multi-cell sandwich tube to be used.

Figure 19

#### 4.2.1 Effect of designing metrics under quasi-static loading

In the above section the FE models of different types of bio-inspired hybrid multi-cell sandwich tubes were validated versus the experimental crush response under quasi-static conditions. Some design parameters including the diameter of the inner tubes and material permutation through a full factorial method in a numerical simulation were considered in order to examine the crushing response of the sandwich tubes. Three different

configurations were designed for use when the external tube diameter was fixed to 80 mm. Table 6 summarizes the geometrical identification and the material specifications.

**Table 6**

The typical load-displacement curves, EA, and SEA of three different configurations correlating to various material permutations are plotted in Figure 20 and the crashworthiness parameters of the parametric study results are summarized in Table 7. In general, specifying Al material to the core tubes has considerable impact on the augmentation of EA, load capacity, and SEA compared to the GFRP core tube. Comparing the MCL, PCL, and EA of each class of material permutation, corresponding to AAA, AAC, CAA, and CAC, revealed that the load capacity and energy absorption were enhanced when the core diameter was decreased and the diameter of the inner tubes alternated between config. 3 and config. 1. Comparing the extracted data for each configuration between AAA and AAC, as presented in Table 7, showed that the average percentage reduction of PCL and MCL were 7% and 11.5%, respectively, except that there was no change in the MCL of config. 2 between the AAA and AAC multi-cell sandwich tubes. Although assigning the GFRP material to the internal tube did not increase the EA, the SEA increased well, especially in the AAC material permutation corresponding to config. 1. In addition, rational CLE, and Ste values of the AAC multi-cell of config. 1 with regular fluctuations of the load displacement curve confirmed better crushing integrity and stable progressive crushing than the AAA and AAC configurations could offer. Comparing AAC and CAA multi-cell tubes, however, produced no remarkable improvement in MCL, in contrast with decreasing the PCL, EA, SEA, CLE, and Ste corresponding to config. 1. Despite a reduction of PCL and MCL between AAC and CAA within config. 2, both material permutations had the same CLE and Ste. The PCL and MCL corresponding to config. 3 of AAC and CAA decreased, such as two other configurations. However, the CLE and Ste increased and the EA and SEA improved. Investigating the trend of CAA load-displacement curve indicated that the sharp drop in the curve was due to the buckling of the inner tubes, followed by a progressive crushing in a small range of displacements and finally the last load drop showed another global buckling in the length of the residual crushing. Thus, it can be concluded that assigning GFRP material to an internal tube plus an external and core Al tube produces the optimal design giving the AAC multi-cell tube better crushing integrity than the EA, SEA, CLE, and Ste. Comparing the results corresponding to each configuration between the AAA, AAC and CAA multi-cells with CAC sandwich tube revealed that lightening the multi-cell tube by replacing the Al internal tubes with GFRP diminishes the efficiency of the energy absorption. According to the load-displacement curve of CAC of config. 1, due to the  $h/d$  and  $d/t$  ratios of the Al core and the weakness of the GFRP tube to prevent the core from buckling everywhere, the MCL, CLE, and Ste decreased considerably. This phenomenon was not present in the two other configurations of CAC. A comparison of configs. 2 and 3, corresponding to CAA and CAC, demonstrates insignificant changes in the

crashworthiness parameters. Thus, the energy absorption efficiency of the CAA and CAC hybrid multi-cell tubes can be differentiated by considering the application. As mentioned at the beginning of this section, sandwiching the internal and external Al with a GFRP core tube considerably reduced the load and EA capacity of the multi-cell tubes. The PCL, MCL and in consequence the CLE decreased since the geometry altered from config. 1 to config 3, while the decline of the PCL and MCL from config. 1 to config. 2 was negligible. The Ste, EA, and SEA decreased first between configs.1 and 2, then increased from config.2 to config.3. Comparing the load-displacement trend of the three configurations correlated to the ACA sandwich tube, and, together with the variety of the EA, showed that changing the geometry from config. 1 to config. 3 made no significant change in the crashworthiness parameters, as presented in Table 7. This the ACA sandwich tube could not improve the crushing behavior of sandwich tubes compared to multi-cell tubes which benefited from an Al core tube. Subsequently, by comparing the ACC and CCA with the ACA sandwich tube indicated that these classes of material permutation did not enhance the crashworthiness parameters, especially the load capacity and SEA. However, the load capacity and EA of CCC were lower than those of the ACA, but the light-weight advantage and space available for crushing and ejecting debris within the CCC structure put the advantages of the SEA, CLE, and Ste significantly higher than those of the ACA sandwich tubes.

Figure 20

**Table 7**

### 4.3 Low velocity axial crushing of the bio-inspired hybrid sandwich tubes:

#### 4.3.1 Experimental low-velocity validation

Bio-inspired multi-cell tubes including ACA, ACC, and CCC were tested under axial low-velocity compression and the load-displacement curves obtained, the corresponding absorbed energy and the SEA of specimens were recalculated and plotted (see Figure 21). All the specimens were impacted by equivalent kinetic energy to 1011.37 J and the crashworthiness indicators correlating to the three multi-cell tubes within the ultimate displacement of each type were compared to the recalculated crashworthiness indicators of the quasi-static test (see Figure 22). No significant enhancement through ACA multi-cell sandwich tube resulted between low-velocity and quasi-static behavior. It can be observed from Figure 23 (a1 and b1), presenting the crush history and morphology of the ACA multi-cell tube, that the two concertina folders of the external Al tube at the initial stage of the quasi-static crushing process were transformed into two areas of diamond deformation; in addition, the diamond deformation of the internal Al tube during the quasi-static condition generated a slightly irregular diamond shape in the low-velocity test. So, it can be inferred that this range of strain rate had a negative effect on the crushing behavior of the Al tubes. Similarly, the same results for single Al tubes were also reported by other researchers [27-29]. Thus, the internal and external tubes in quasi-static conditions induced

more perpendicular stress on the GFRP core tubes, quickly followed by normal directional breaking of these tubes. Eventually the PCL increased to 25% leading to a lower CLE value and feeble crushing integrity. The response of the ACC multi-cell tube was completely different. In this material permutation, the initial concertina folding of the external Al tube under low-velocity compression kept constant; additionally, the results demonstrated that the load capacity and EA efficiency increased considerably beyond those in quasi-static conditions due to the strain rate effects on the thermoset composite tube [54, 55]. These phenomena caused the reduction of the perpendicular load at the joint surface of the AL and GFRP tubes: where the normal directional breaking of GFRP tubes did not occur and the dominance of the plastic deformation of Al tube on GFRP tubes was dissipated. According to Figure 23 (a2 and b2), the GFRP tubes were progressively crushed, and consequently inter-laminar delamination and fiber breakage ensued in each GFRP tube, followed by noticeable improvement in the crashworthiness parameters (see Figure 22). It is worth mentioning that the hybridization of the external Al tube with inner GFRP tubes increased the MCL of the ACC multi-cell tube compared to quasi-static MCL values, resulting in a higher CLE of the ACC through low-velocity experimentation. Yet assigning GFRP as the external tube instead of Al (the CCC multi-cell tube) increased the PCL and MCL to 132% and 72%, respectively. The principal damage mechanisms of the CCC multi-cell sandwich tube under low-velocity compression were intra-laminar and inter-laminar delamination. The contact load between the GFRP tube walls declined lower than in quasi-static conditions, which induced more progressive crushing failure instead of the combination of progressive crushing and normal directional breaking of GFRP tubes. In particular, the existence of circumferential cracks propagated in the first crushing stage of the quasi-static test were not observed in Figure 23 (a3 and b3). When specimens were tested under low velocity compression, the friction between the plies due to inter-laminar delamination was more marked than in quasi-static conditions. Thus, the strain rate effect and the improvement of the progressive crushing mechanisms of the GFRP tubes resulted in higher EA and load capacity than were available in quasi-static conditions. According to the above descriptions of failure mechanisms and strain rate effects of the Al and GFRP tubes, the CCC multi-cell tube had higher Ste, MCL, and EA than either the ACA or the ACC specimens. Thus, the SEA and the relevant increasing percentage of CCC were about 60% and the ACA was lower in value. It is worth noting that the AES of the ACA reduced by about 75 % while the AES of the ACC and the CCC multi-cell tubes increased by 247% and 177% respectively, indicating the effect of GFRP tubes on increasing the stroke efficiency under similar kinetic energy.

#### *4.3.2 Strain rate effect on the GFRP material model*

The crushing mechanisms of the GFRP tubes including fiber breaking, fragmentation and the delamination of material are classified as micro-scale damaging, since the failure process through the Enhanced Composite Damage material model (\*MAT\_54) in LS-DYNA was based on linking the developed stresses and strains to the

ultimately defined strengths and strains from the macro-scale perspective. Thus, it would be useful to consider these micro-scale effects, such as the high energy absorption of the GFRP tubes through fiber breaking and fragmentation, at intermediate strain rates into the FE material model, since this material model was formulated from the macro-scale perspective. In other words, due to the continuous formulating base of the FE material model, this model is inefficient when it comes to diagnosing the reasons for the sudden failure of the material continuum from the micro-scale perspective at a low-velocity strain rate. Subsequently, the crush-front elements fail prematurely, followed by declining energy absorption and load capacity during the crushing process. According to previous studies [54, 55], the elastic modulus and ultimate strengths of GFRP did not change due to the strain rate in the range of  $[10^{-4}-10^3]$ , but the failure strains including the ultimate strains increased significantly. This phenomenon has been observed with greater precision in woven fiber sheets [54]. Thus, the approach of calibrating the failure strains was taken to ensure that the elements did not face premature failure and, simultaneously, that the contact between the crash-front elements and the impactor remained unbroken. This resulted in increased internal energy and a progressive failure mechanism of GFRP within the multi-cell sandwich tubes. So, the three main strain failure modes of DFAILT, DFAILC, and DFAILM were adopted for re-parameterization and the final values are presented in Table 8. It is worth mentioning that during the calibration process, DFAILC showed significant effects in achieving a proper trend of the load-displacement curve and failure mechanisms of the GFRP tubes.

**Table 8**

The FE analysis (FEA) of the low-velocity response of ACA, ACC, and CCC multi-cell sandwich tubes was compared to experiments as depicted in Figures 21 and 23. The predicted load-displacement and energy-displacement curves of the numerical model correlated a desirable trend with the experimental results; moreover, the calculated MCL, PCL, CLE, and Ste of the three multi-cell sandwich tubes accorded well with the experiments and the maximum error corresponding to the EA value of the ACA sandwich tube was about 10.6%. By comparing the snapshots of the crushed multi-cell sandwich tubes presented in Figure 23, it is clear that the FE model can illustrate the failure patterns of the AL and GFRP tubes. In one instance (see Figure 23 (b2 and c2)), the deformation of the external Al tube of ACC sandwich tube is in diamond mode with 4 corners ( $N=4$ ); this deformation pattern can also be observed in the FE model. The FE model can show the delamination and fiber breaking of inner GFRP tubes with suitable correlation to low-velocity tests.

Figure 21

Figure 22

Figure 23

#### 4.3.3 *Effect of designing metrics under low-velocity loading:*

In the last section of this study, after investigating the low-velocity response of ACA, ACC, and CCC multi-cell sandwich tubes and comparing the results with quasi-static responses, the FE model was developed by calibrating the ultimate strains, having considered the strain rate effects on the GFRP material model. Next, the effects of permutations of inner tube diameters and different materials on the crashworthiness parameters and failure mechanisms were assessed through numerical parametric study. To this end, the simulation corresponding to quasi-static loading was re-adopted and an initial velocity equal to 6.609 m/s, the same as the velocity in practice, was applied to the upper rigid platen. The crashworthiness parameters related to the numerical parametric study of low-velocity response are presented in Table 9. The pattern for altering the crashworthiness parameters of different material permutations by introducing three configurations are seen to be similar to the pattern with a quasi-static response. The multi-cell sandwich tubes with Al core still have higher-value EA and load bearing capacity than those with a GFRP core. By comparing the crashworthiness indicators of the sandwich tubes containing an Al core, it can be concluded that, due to the higher CLE values, the sandwich tubes designed within config. 1 had suitable crashworthiness indicators and integrity when crushed. Although the config. 1 of the AAC performed better under quasi-static compression, the config. 1 of the CAC revealed optimal crashworthiness characteristics under a low-velocity loading. The values of CLE, EA, and SEA of this class of multi-cell sandwich tube indicated better crush integrity and energy absorption efficiency than could the other configurations of CAC and the other classes of material permutation with different configurations.

In the following, the config. 1 of the AAC sandwich tube revealed higher load bearing capacity and energy absorption efficiency. The config. 1 of this material permutation had higher CLE, Ste, and SEA than any other class of sandwich tube, especially the AAA and CAA sandwich tubes, denoting acceptable crushing integrity. However, the sandwich tubes containing the GFRP core had lower load bearing capacity and energy absorption than those with an Al core, but the config. 1 of the ACA sandwich tubes presented optimal crashworthiness parameters, including EA, SEA, and Ste, which were approximately equal to the CAA and AAC; moreover, the CLE value of this class of sandwich tube showed suitable crushing integrity.

Subsequently, the calculated low-velocity crashworthiness parameters of different types of multi-cell sandwich tubes such as the PCL, MCL, EA, and SEA values, were calculated and compared with the corresponding values of quasi-static conditions in the same displacement (see Figure 24). It can be seen from Figure 24 (a) that the PCL of all the simulated sandwich tubes increased beyond that for quasi-static loading. In contrast the MCL of some types of sandwich tube decreased or remained constant. This reduction occurred in three other classes of multi-cell sandwich tube, namely, 1-config. 1 of the CAA; 2-configs. 2 and 3 of the AAA, CAA, and CAC; 3-config. 3 of the AAC and ACA. This phenomenon resulted in the reduction of the EA and SEA values of these

sandwich tubes. The deformation modes of the Al tubes in the ACA specimens under low-velocity loadings were transformed from concertina to diamond mode due to the effects of the  $h/d$  and  $d/t$  ratios of the Al tubes.

**Table 9**

Thus, the interaction load between the components declined and induced the decline of the MCL and EA from their quasi-static response. With the effects of the  $h/d$  and  $d/t$  ratios in mind, the reason for mitigating the MCL in the AAA, AAC, CAA, and CAC was investigated (see Figures 25-26). In Figure 25, the crushing modes of the above sandwich tubes were compared with those of the quasi-static response in two similar stages including the initial stage of the crushing process and the second, the ultimate displacement of the low-velocity process. As can be observed in the initial stage of quasi-static compression (QS-1) of configs. 2 and 3 of the AAA (Figure 25 (a)), the crushing of the sandwich tube started from both ends. In this stage the external and internal tubes folded from the upper end and the core tube folded from the lower end. This incident caused increased interaction load among the components. While these components began to be crushed, the lower end at the same stage of low-velocity condition (LV-1) showed a lower interaction load (see Figure 26 (a)) and higher PCL values. This deformation pattern was continued until the ultimate displacement (QS-2 and LV-2) and the MCL of the low-velocity response declined below that of the quasi-static one. The higher  $h/d$  and  $d/t$  ratios of the Al core in the config. 3 of the AAA comparing to config. 2, resulted in a greater decline of MCL and further increment of PCL. These kinds of interaction behavior were also observed in sandwich tubes with two adjacent AL tubes such as AAC, CAA (see Figures 25 and 26 (b-c)). As can be seen from Figure 25 (b) corresponding to config. 3 of the AAC, the resistance of the internal GFRP tube to normal directional breaking, the interaction between components, and the deformation in response of the components in the QS-1 and QS-2 stages were completely different from the interaction and independent deformation process of components in the LV-1 and LV-2 stages. In other words, the folding of the external and core tubes occurred in equal steps infiltrated in one another's gaps. Thus, the interaction load (Figure 26 (b)) and subsequently the MCL declined unlike the quasi-static response. It is worth mentioning that in the QS-1 stage corresponding to config. 1 of the CAA, the Al core prevented the global buckling of the internal tube in the lower part of the structure, in contrast with the independent crushing behavior of the core and internal tube in the LV-1 stage. Additionally, when a perpendicular load was applied on the external GFRP tube due to the deformation process of the core at the D-2 stage, a catastrophic failure occurred in the lower part of the external GFRP tube, in contrast with the progressive crushing found at the QS-2 stage. These behaviors can be seen in the two other configurations of the CAA; in addition, the  $h/d$  and  $d/t$  ratios increased and infiltration of the folders of the Al tubes caused more reduction of MCL because the core diameter was increasing. From config. 3 of the ACA snapshots presented in Figure 25 (d), the internal Al tube initiated the crushing from both ends, unlike the crushing at one end of the external Al tube

at the QS-1 stage. At the QS-2 stage, due to the deformation pattern of the Al tubes and progressive crushing of the GFRP core, the interaction load between the components increased (see Figure 26 (d)). In contrast, the internal and external Al tubes at the LV-1 stage folded respectively from the top end and from the bottom. The crushing of the bottom end of the external Al tube caused shear cracks to propagate in the GFRP core. Thus, the growth ratio of the interaction load corresponded to the decreased ACA sandwich tube compared to the quasi-static compression. In configs. 2 and 3 of the CAC sandwich tube (Figures 25-26 (e)), the initiation of the crushing corresponded to the low-velocity compression of the external and internal parts of the GFRP tube (LV-1 and LV-2) at the two ends compared to the crushing process in quasi-static conditions (QS-1 and QS-2). This incident, also observed in other cases, resulted in the reduction of the interaction load (see Figure 26 (e)) and the MCL values and the increment in the PCL values. As a preliminary conclusion, although the multi-cell sandwich tubes containing Al core had greater load bearing capacity and energy absorption, they did not have proper crashworthiness indicators or behavior upon crushing. Moreover, due to the strain rate effects on the GFRP tube, multi-cell sandwich tubes consisting of more GFRP components such as ACC, CCA and CCC showed improved low-velocity behavior.

Figure 24

Figure 25

Figure 26

## 5. Conclusion

Efficient and novel designs of composite materials and hybrid multi-cell structures are practicable if a bio-inspired approach is adopted. In this study, the crushing response of novel bio-mimicked multi-cell sandwich tubes with the hierarchical core is mainly investigated under quasi-static and low-velocity compression by executing a series of material permutations including ACA, ACC, and CCC experimentally. For understanding the effects of the diverse material permutation and the diameter of the internal tubes on the energy absorption response of the bio-inspired multi-cell sandwich tubes, numerical parametric studies were conducted based on validating FE models versus the experimental quasi-static and low-velocity response of single hollow tubes and multi-cell sandwich tubes. The findings lead mainly to the following conclusions:

The hybridization of Al and GFRP tubes was proposed to improve the crashworthiness characteristics and failure modes, especially the behavior under the crushing of the external Al tube with its higher  $h/d$  and  $d/t$  ratios. Packing external Al tubes with internal and core composite ones (ACC sandwich tube) caused the external Al tube to show more concertina folding patterns than the irregular diamond mode, having observed in the ACA sandwich tube and corresponded single hollow tube. This phenomenon induced lower normal breaking load between composite and Al components where inter-laminar and intra-laminar delamination and transversal fiber breakage were the dominant crushing modes instead of the normal breaking

mechanism. By contrast, the inner GFRP tubes of the CCC specimen underwent a stable and progressive crushing mode because the normal breaking interaction load was alleviated entirely. Although the load-bearing capacity and energy absorption of the ACA multi-cell sandwich tube are greater than those of the ACC and CCC, the SEA, CLE, and Ste of CCC specimen were considerably higher than either the ACC or the ACA.

At the same time, conducting a low-velocity test on the manufactured specimen, namely, the ACA, ACC, and CCC, revealed the significant influence of the strain rate on the GFRP tubes in contrast with AL tubes. The external Al tubes in the ACA specimen folded irregularly than did the quasi-static compression with equal displacement. This phenomenon caused an increment in the PCL without any significant improvement in the MCL, EA, or SEA. Due to the strain rate effect on the GFRP tubes corresponding to the CCC multi-cell sandwich tube, the increasing percentages of PCL, MCL, EA, and SEA were noticeable, such that the level of load-bearing capacity and crashworthiness indicators was equivalent to the ACC hybrid multi-cell sandwich tube and much higher than those of ACA specimen. In addition, the combination of normal directional breaking and progressive crushing of the inner GFRP tubes were transmuted into pure progressive crushing dominated by inter-laminar delamination and transversal fiber breakage.

The numerical parametric study of quasi-static conditions indicated that the multi-cell sandwich tubes containing the Al core tube had significantly higher energy absorption and load-bearing capacity than those consisting of the GFRP core tube, especially with the config.3. Generally, the config.1 of the AAC had the optimal crashworthiness characteristics, stable and progressive failure mechanisms (the Ste was 74.58%), better crushing integrity, and regular fluctuations of the load-displacement curve among all the multi-cell sandwich tubes; so that the corresponded SEA, CLE, and EA values were 26.57 J/gr, 72.45%, and 5521.32 J.

The low-velocity numerical parametric study revealed that the crashworthiness parameters of specimens containing an Al core remained higher than those consisting of GFRP core tubes. Nevertheless, due to the improper behavior of the Al tubes within this bio-inspired geometry under intermediate strain rate, the crashworthiness indicators, except for the PCL, declined such that the reduction of the MCL, EA, and SEA was more significant in config.3 of specimens with Al core. Additionally, the perceptible strain rate effects on an E/glass composite manifested that increasing the number of GFRP components strengthened the crashworthiness of multi-cell sandwich tubes such as the ACC, CCA, and CCC. By considering the crashworthiness parameters and the improved crushing behavior compared to the quasi-static compression simultaneously, the config.2 of the CCC showed suitable alteration compared to quasi-static condition whereas the SEA, EA increased up to 58%. On the other hand, config.1 of AAC still owned higher

crashworthiness indicators such that the SEA, EA, and CLE are calculated as 4.15 J/gr, 935.66 J, and 79.84%.

## 6. References

- [1] Moeinifard M, Liaghat G, Rahimi G, Talezadehlari A, Hadavinia H. Experimental investigation on the energy absorption and contact force of unstiffened and grid-stiffened composite cylindrical shells under lateral compression. *Composite Structures*. 2016;152:626-36.
- [2] Kılıçaslan C, Güden M, Odacı İK, Taşdemirci A. Experimental and numerical studies on the quasi-static and dynamic crushing responses of multi-layer trapezoidal aluminum corrugated sandwiches. *Thin-Walled Structures*. 2014;78:70-8.
- [3] Abosbaia A, Mahdi E, Hamouda A, Sahari B, Mokhtar A. Energy absorption capability of laterally loaded segmented composite tubes. *Composite Structures*. 2005;70:356-73.
- [4] Jia X, Chen G, Yu Y, Li G, Zhu J, Luo X, et al. Effect of geometric factor, winding angle and pre-crack angle on quasi-static crushing behavior of filament wound CFRP cylinder. *Composites Part B: Engineering*. 2013;45:1336-43.
- [5] Eshkoo R, Oshkoo S, Sulong A, Zulkifli R, Ariffin A, Azhari C. Effect of trigger configuration on the crashworthiness characteristics of natural silk epoxy composite tubes. *Composites Part B: Engineering*. 2013;55:5-10.
- [6] Hosseini SM, Shariati M. Experimental analysis of energy absorption capability of thin-walled composite cylindrical shells by quasi-static axial crushing test. *Thin-Walled Structures*. 2018;125:259-68.
- [7] Ochelski S, Gotowicki P. Experimental assessment of energy absorption capability of carbon-epoxy and glass-epoxy composites. *Composite Structures*. 2009;87:215-24.
- [8] Pickett L, Dayal V. Effect of tube geometry and ply-angle on energy absorption of a circular glass/epoxy crush tube—a numerical study. *Composites Part B: Engineering*. 2012;43:2960-7.
- [9] Palanivelu S, Van Paepegem W, Degrieck J, Vantomme J, Kakogiannis D, Van Ackeren J, et al. Crushing and energy absorption performance of different geometrical shapes of small-scale glass/polyester composite tubes under quasi-static loading conditions. *Composite Structures*. 2011;93:992-1007.
- [10] Taghizadeh S, Farrokhabadi A, Liaghat G, Pedram E, Malekinejad H, Mohammadi SF, et al. Characterization of compressive behavior of PVC foam infilled composite sandwich panels with different corrugated core shapes. *Thin-Walled Structures*. 2019;135:160-72.
- [11] Niknejad A, Abedi MM, Liaghat GH, Nejad MZ. Prediction of the mean folding force during the axial compression in foam-filled grooved tubes by theoretical analysis. *Materials & Design*. 2012;37:144-51.
- [12] Niknejad A, Elahi SA, Liaghat GH. Experimental investigation on the lateral compression in the foam-filled circular tubes. *Materials & Design (1980-2015)*. 2012;36:24-34.
- [13] Rezaei B, Niknejad A, Assaee H, Liaghat G. Axial splitting of empty and foam-filled circular composite tubes—An experimental study. *Archives of Civil and Mechanical Engineering*. 2015;15:650-62.
- [14] Lin J, Wang X, Fang C, Huang X. Collapse loading and energy absorption of fiber-reinforced conical shells. *Composites Part B: Engineering*. 2015;74:178-89.
- [15] Kalhor R, Akbarshahi H, Case SW. Numerical modeling of the effects of FRP thickness and stacking sequence on energy absorption of metal–FRP square tubes. *Composite Structures*. 2016;147:231-46.
- [16] Kim J-S, Yoon H-J, Shin K-B. A study on crushing behaviors of composite circular tubes with different reinforcing fibers. *International Journal of Impact Engineering*. 2011;38:198-207.
- [17] Taghizadeh SA, Naghdinasab M, Madadi H, Farrokhabadi A. Investigation of novel multi-layer sandwich panels under quasi-static indentation loading using experimental and numerical analyses. *Thin-Walled Structures*. 2021;160:107326.
- [18] Eyvazian A, Moeinifard M, Musharavati F, Taghizadeh SA, Mahdi E, Hamouda AM, et al. Mechanical behavior of resin pin-reinforced composite sandwich panels under quasi-static

indentation and three-point bending loading conditions. *Journal of Sandwich Structures & Materials*. 2020;1099636220909752.

- [19] Zhang Z, Sun W, Zhao Y, Hou S. Crashworthiness of different composite tubes by experiments and simulations. *Composites Part B: Engineering*. 2018;143:86-95.
- [20] El-Hage H, Mallick P, Zamani N. A numerical study on the quasi-static axial crush characteristics of square aluminum-composite hybrid tubes. *Composite Structures*. 2006;73:505-14.
- [21] Liu Q, Xu X, Ma J, Wang J, Shi Y, Hui D. Lateral crushing and bending responses of CFRP square tube filled with aluminum honeycomb. *Composites Part B: Engineering*. 2017;118:104-15.
- [22] Guler MA, Cerit ME, Bayram B, Gerceker B, Karakaya E. The effect of geometrical parameters on the energy absorption characteristics of thin-walled structures under axial impact loading. *International Journal of Crashworthiness*. 2010;15:377-90.
- [23] Liu Q, Ma J, He Z, Hu Z, Hui D. Energy absorption of bio-inspired multi-cell CFRP and aluminum square tubes. *Composites Part B: Engineering*. 2017;121:134-44.
- [24] Huang J, Wang X. Numerical and experimental investigations on the axial crushing response of composite tubes. *Composite Structures*. 2009;91:222-8.
- [25] Wu Y, Liu Q, Fu J, Li Q, Hui D. Dynamic crash responses of bio-inspired aluminum honeycomb sandwich structures with CFRP panels. *Composites Part B: Engineering*. 2017;121:122-33.
- [26] Zhu G, Sun G, Yu H, Li S, Li Q. Energy absorption of metal, composite and metal/composite hybrid structures under oblique crushing loading. *International Journal of Mechanical Sciences*. 2018;135:458-83.
- [27] Wierzbicki T. Axial resistance and energy absorption of externally reinforced metal tubes. *Composites Part B: Engineering*. 1996;27:387-94.
- [28] Hsu S, Jones N. Quasi-static and dynamic axial crushing of thin-walled circular stainless steel, mild steel and aluminium alloy tubes. *International Journal of Crashworthiness*. 2004;9:195-217.
- [29] Abramowicz W, Jones N. Dynamic axial crushing of circular tubes. *International Journal of Impact Engineering*. 1984;2:263-81.
- [30] Kumar AP, Manieah D. Deformation studies on the significance of combined geometry tubes as energy absorbing structures. *Int J Civil Eng Technol*. 2019;10:2812-20.
- [31] Eyvazian A, Mozafari H, Hamouda AM. Experimental study of corrugated metal-composite tubes under axial loading. *Procedia engineering*. 2017;173:1314-21.
- [32] Mamalis A, Manolakos D, Demosthenous G, Ioannidis M. Energy absorption capability of fibreglass composite square frusta subjected to static and dynamic axial collapse. *Thin-Walled Structures*. 1996;25:269-95.
- [33] Palanivelu S, Van Paeppegem W, Degrieck J, Van Ackeren J, Kakogiannis D, Van Hemelrijck D, et al. Experimental study on the axial crushing behaviour of pultruded composite tubes. *Polymer Testing*. 2010;29:224-34.
- [34] Zhang L, Bai Z, Bai F. Crashworthiness design for bio-inspired multi-cell tubes with quadrilateral, hexagonal and octagonal sections. *Thin-Walled Structures*. 2018;122:42-51.
- [35] San Ha N, Lu G. A review of recent research on bio-inspired structures and materials for energy absorption applications. *Composites Part B: Engineering*. 2020;181:107496.
- [36] Chen B, Zou M, Liu G, Song J, Wang H. Experimental study on energy absorption of bionic tubes inspired by bamboo structures under axial crushing. *International Journal of Impact Engineering*. 2018;115:48-57.
- [37] Xiao Y, Yin H, Fang H, Wen G. Crashworthiness design of horsetail-bionic thin-walled structures under axial dynamic loading. *International Journal of Mechanics and Materials in Design*. 2016;12:563-76.
- [38] Ying L, Gao T, Hou W, Dai M, Han X, Jiang D. On crashing behaviors of bio-inspired hybrid multi-cell Al/CFRP hierarchical tube under quasi-static loading: An experimental study. *Composite Structures*. 2021;257:113103.
- [39] Hussein RD, Ruan D, Lu G, Thomson R. An energy dissipating mechanism for crushing square aluminium/CFRP tubes. *Composite Structures*. 2018;183:643-53.
- [40] Dlugosch M, Fritsch J, Lukaszewicz D, Hiermaier S. Experimental investigation and evaluation of numerical modeling approaches for hybrid-FRP-steel sections under impact loading for the application in automotive crash-structures. *Composite Structures*. 2017;174:338-47.
- [41] Safri SNA, Sultan MTH, Jawaid M, Jayakrishna K. Impact behaviour of hybrid composites for structural applications: A review. *Composites Part B: Engineering*. 2018;133:112-21.

- [42] Wang Z, Jin X, Li Q, Sun G. On crashworthiness design of hybrid metal-composite structures. *International Journal of Mechanical Sciences*. 2020;171:105380.
- [43] Song H-W, Wan Z-M, Xie Z-M, Du X-W. Axial impact behavior and energy absorption efficiency of composite wrapped metal tubes. *International Journal of Impact Engineering*. 2000;24:385-401.
- [44] Bouchet J, Jacquelin E, Hamelin P. Dynamic axial crushing of combined composite aluminium tube: the role of both reinforcement and surface treatments. *Composite Structures*. 2002;56:87-96.
- [45] Liu W, Lin Z, He J, Wang N, Deng X. Crushing behavior and multi-objective optimization on the crashworthiness of sandwich structure with star-shaped tube in the center. *Thin-Walled Structures*. 2016;108:205-14.
- [46] Isaac CW, Ezekwem C. A review of the crashworthiness performance of energy absorbing composite structure within the context of materials, manufacturing and maintenance for sustainability. *Composite Structures*. 2020:113081.
- [47] El-Hage H, Mallick P, Zamani N. A numerical study on the quasi-static axial crush characteristics of square aluminum tubes with chamfering and other triggering mechanisms. *International Journal of Crashworthiness*. 2005;10:183-96.
- [48] Gladman B. LS-DYNA® keyword user's manual–Volume II–Material Models. Livermore, CA: Livermore Software Technology Corporation. 2013.
- [49] Mohamed MN, Kumar AP. Numerical and experimental study of the effect of orientation and stacking sequence on petalling of composite cylindrical tubes under axial compression. *Procedia engineering*. 2017;173:1407-14.
- [50] Han H, Taheri F, Pegg N, Lu Y. A numerical study on the axial crushing response of hybrid pultruded and  $\pm 45^\circ$  braided tubes. *Composite Structures*. 2007;80:253-64.
- [51] Taherzadeh-Fard A, Liaghat G, Ahmadi H, Razmkhah O, Charandabi SC, Zarezadeh-mehrzi MA, et al. Experimental and numerical investigation of the impact response of elastomer layered fiber metal laminates (EFMLs). *Composite Structures*. 2020;245:112264.
- [52] Guillow S, Lu G, Grzebieta R. Quasi-static axial compression of thin-walled circular aluminium tubes. *International Journal of Mechanical Sciences*. 2001;43:2103-23.
- [53] Farley GL. Relationship between mechanical-property and energy-absorption trends for composite tubes: National Aeronautics and Space Administration, Office of Management ..., 1992.
- [54] Harding J, Welsh LM. A tensile testing technique for fibre-reinforced composites at impact rates of strain. *Journal of materials science*. 1983;18:1810-26.
- [55] Reuter C, Sauerland K-H, Tröster T. Experimental and numerical crushing analysis of circular CFRP tubes under axial impact loading. *Composite Structures*. 2017;174:33-44.

## Figures:

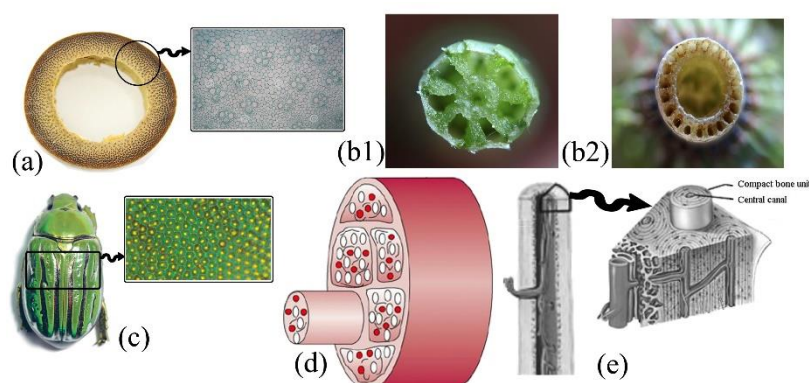


Figure 2: Illustration of biological structures inspiring bio-mimetic energy absorbers a) bamboo, b) horsetail, c) beetle, d) human vessel, e) human bone

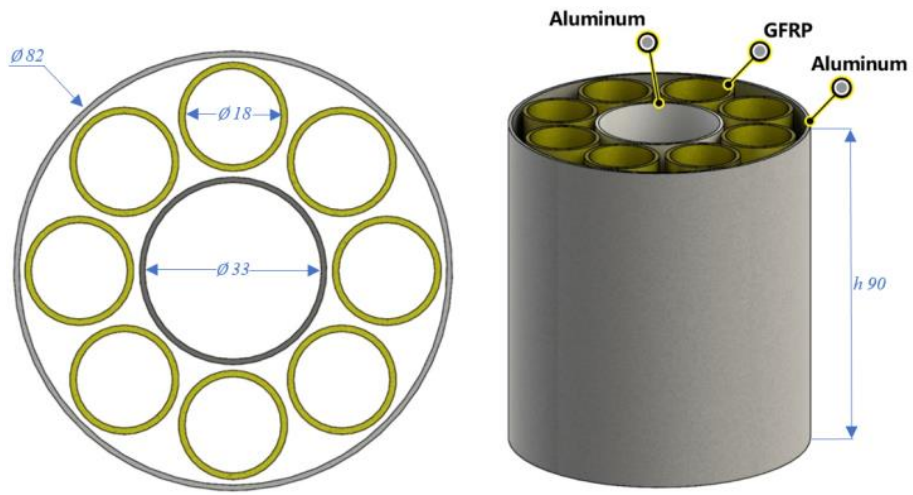


Figure 2: Schematic of a manufactured bio-inspired hybrid multi-cell sandwich tube (ACA).

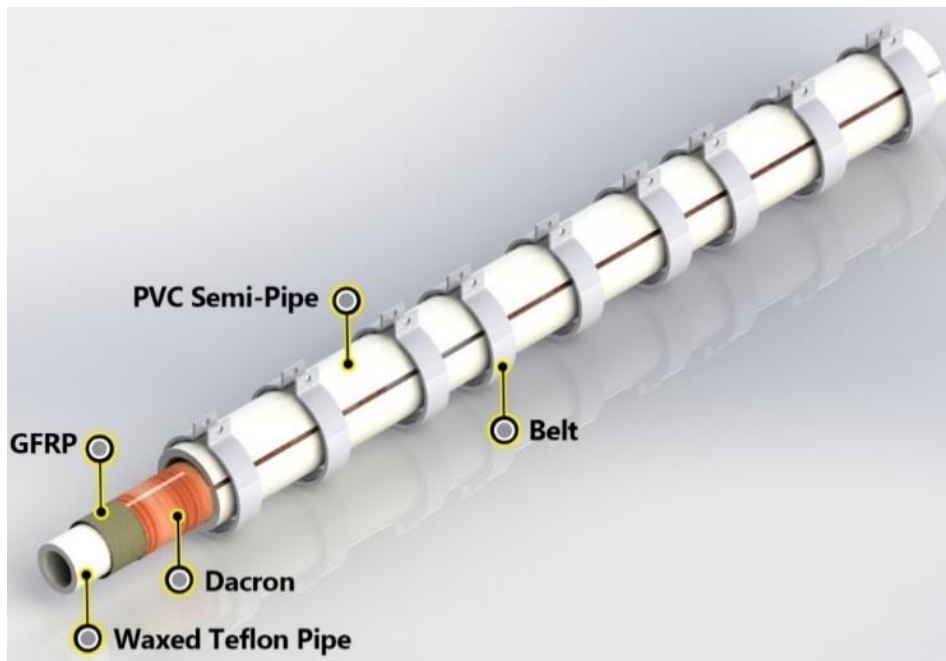


Figure 3: Sample fabrication through the improved hand laying up method.

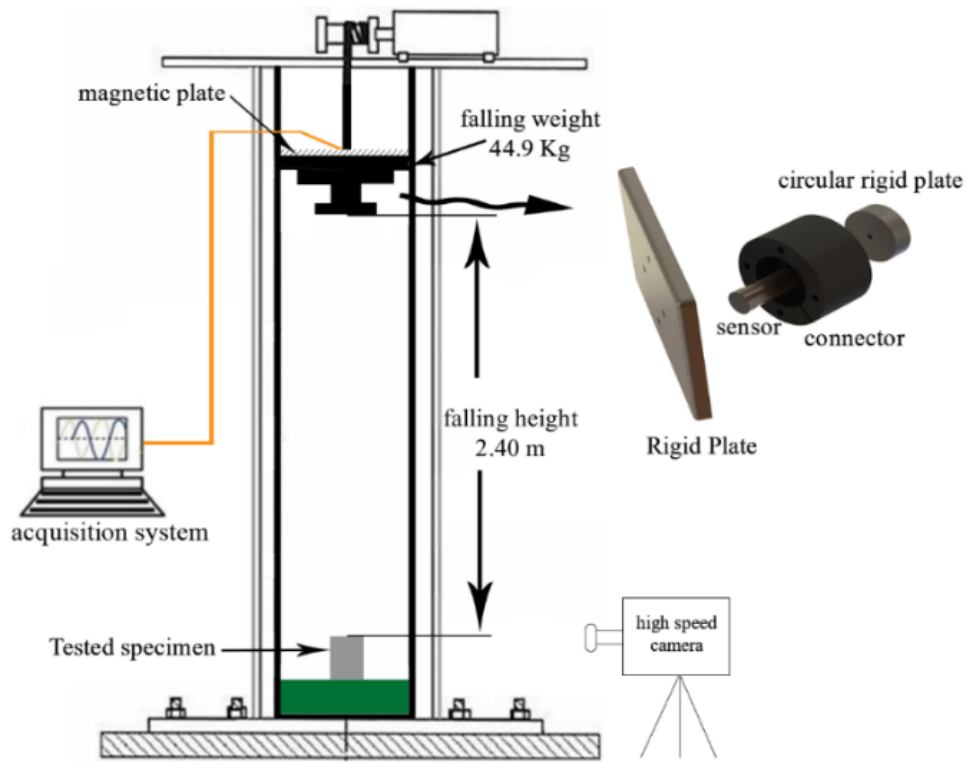


Figure 4: drop weight test setup.

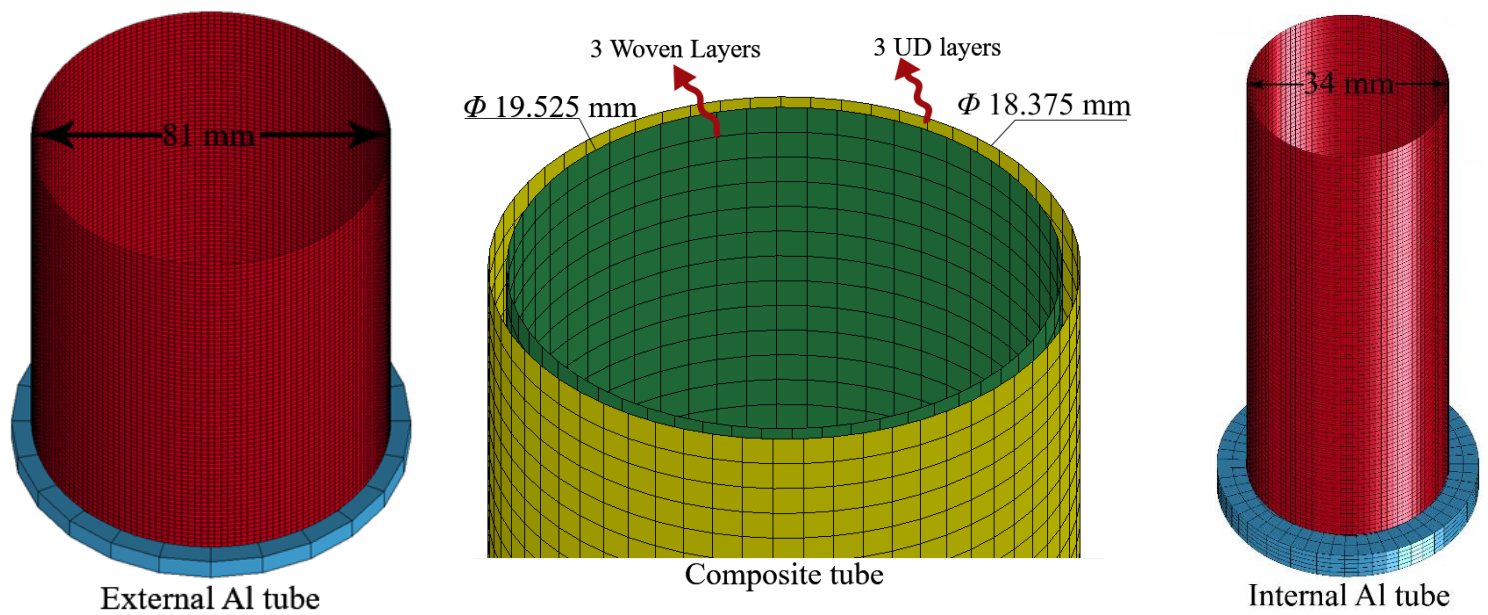


Figure 5: Simulated aluminum and composite tubes under quasi-static compression loading.

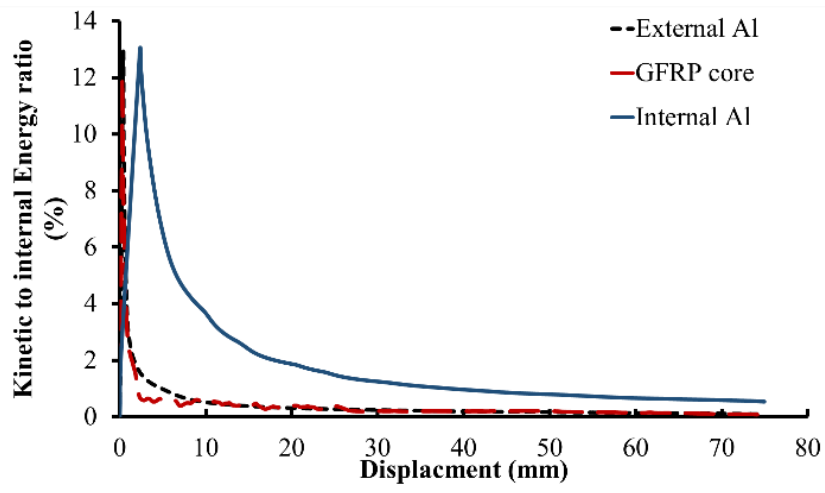


Figure 6: Ratio of the kinetic to internal energy versus displacement of the individual tubes

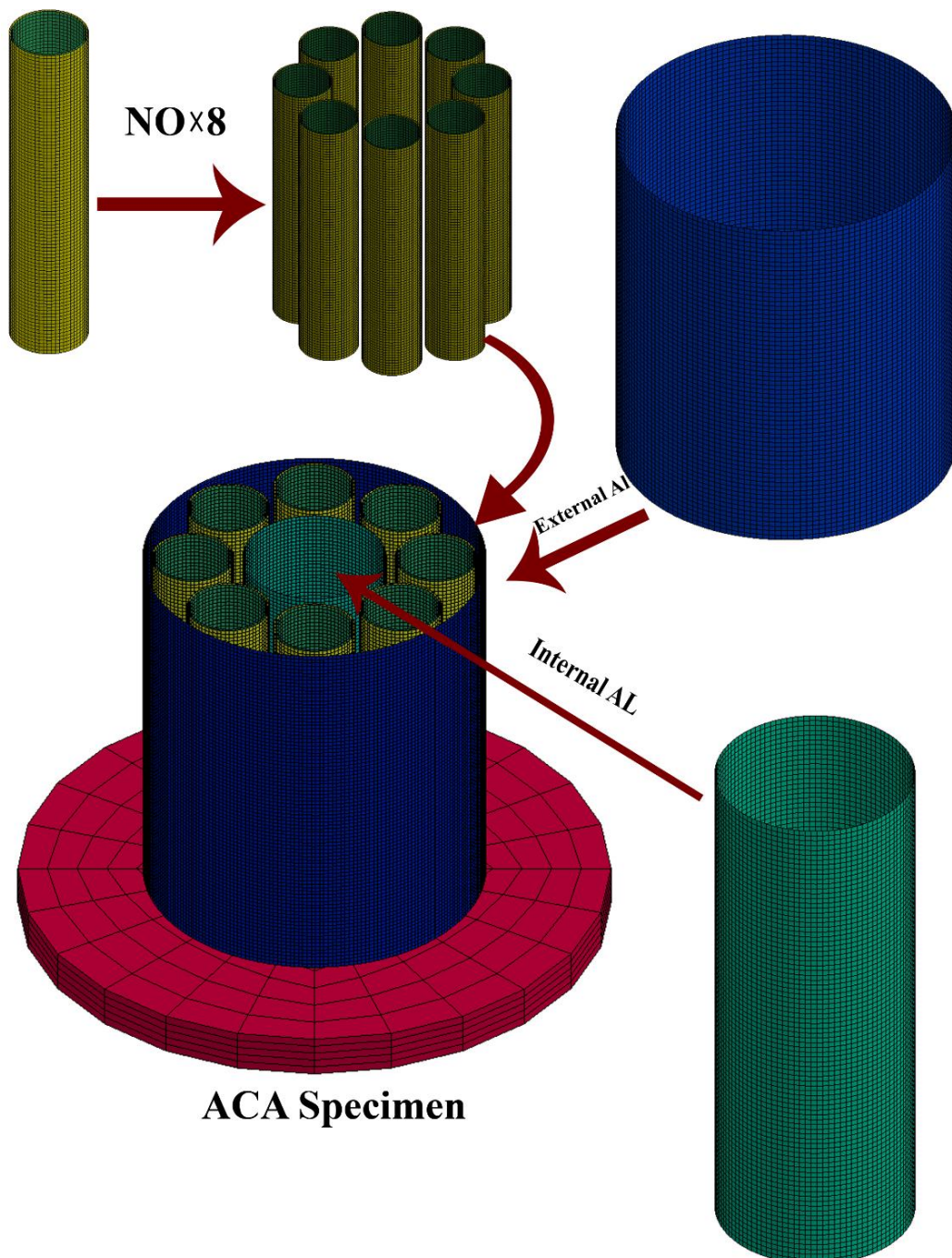


Figure 7: Simulation of the complete geometry of the bio-inspired hybrid multi-cell sandwich tube (ACA)

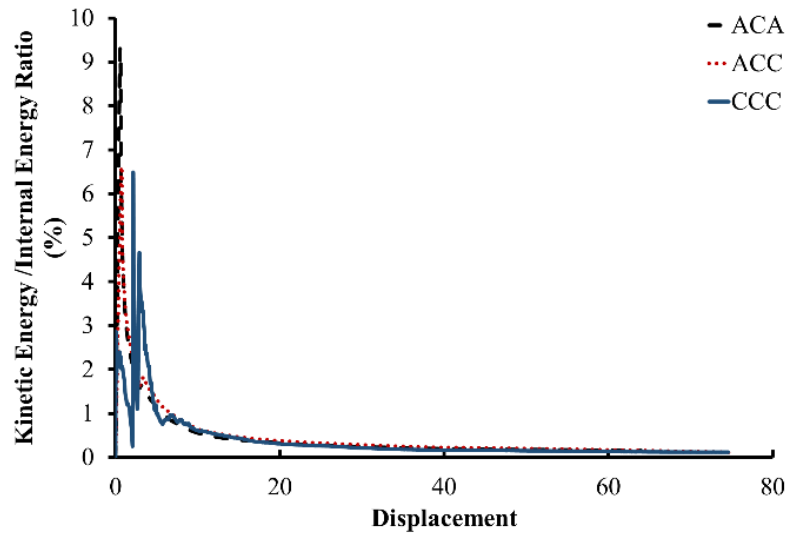


Figure 8: Ratio of the kinetic to internal energy versus displacement of hybrid multi-cell sandwich tubes.

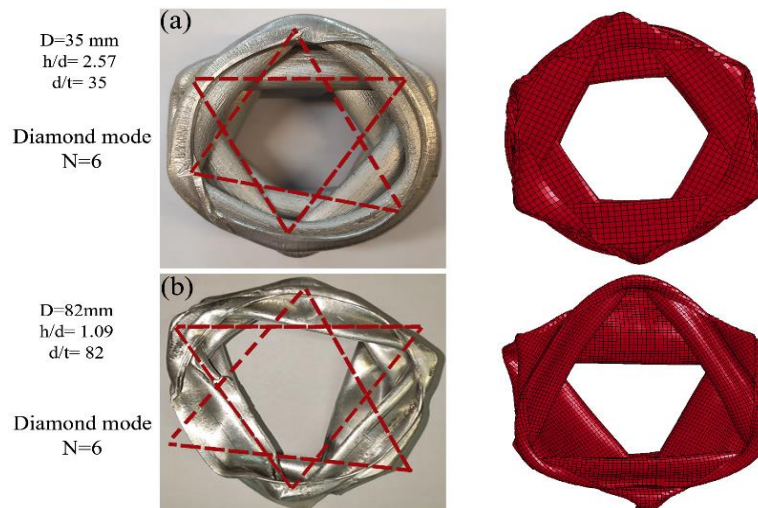


Figure 9: Comparative deformation modes of Al tubes under axial crushing: (a) internal and (b) external tube.

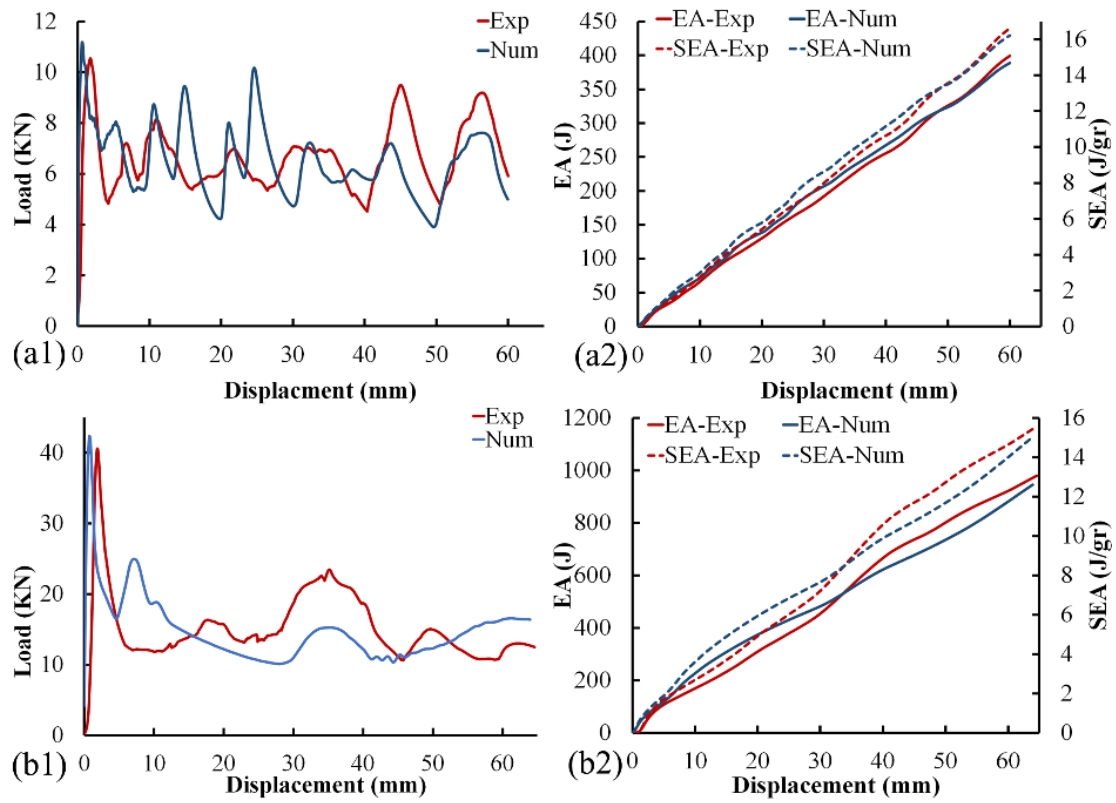


Figure 10: Load-displacement and corresponding absorbed energy and SEA of Al tube: (a) internal, and (b) external.

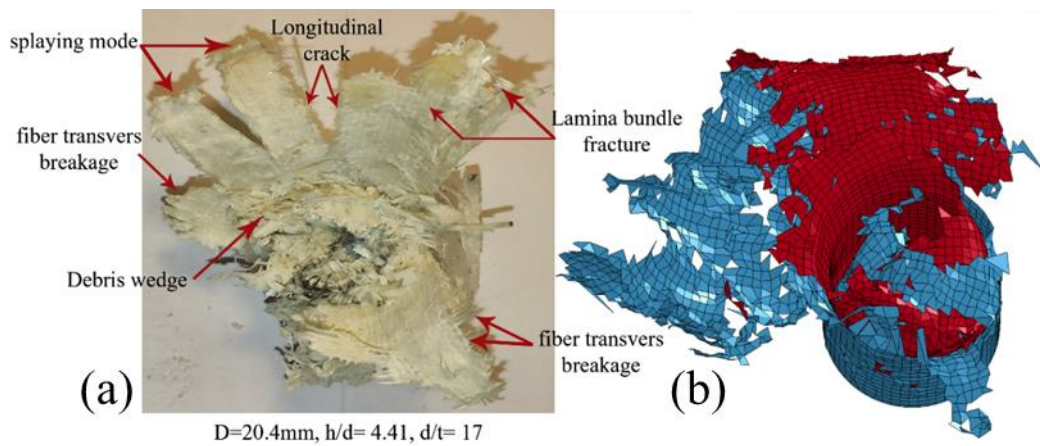


Figure 11: Comparative post crushed damage morphologies of (a) experiment and (b) predictions of FEM.

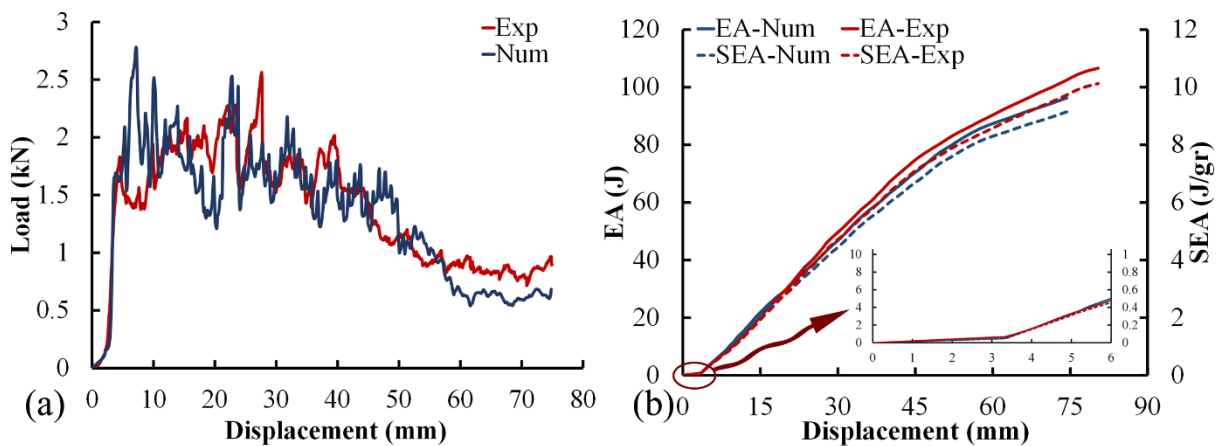


Figure 12: Load-displacement and corresponding absorbed energy and SEA of the GFRP composite tube.

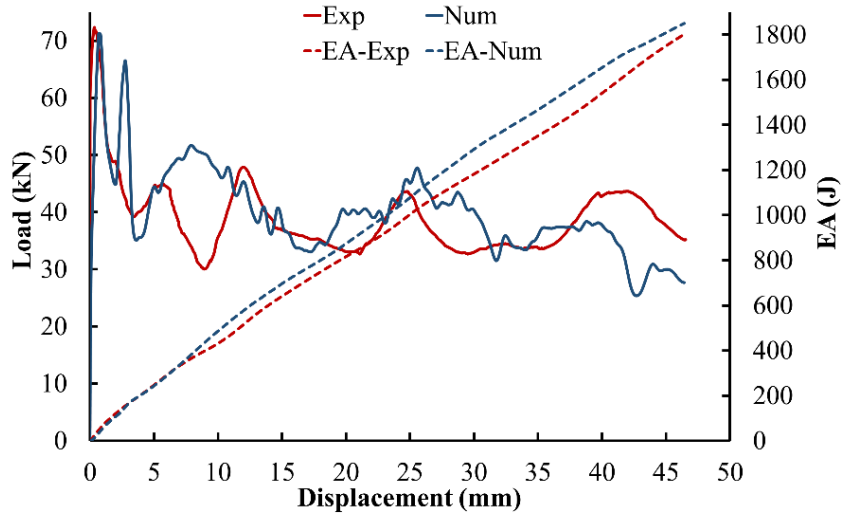


Figure 13: obtained load-displacement and corresponding EA of ACA specimens.

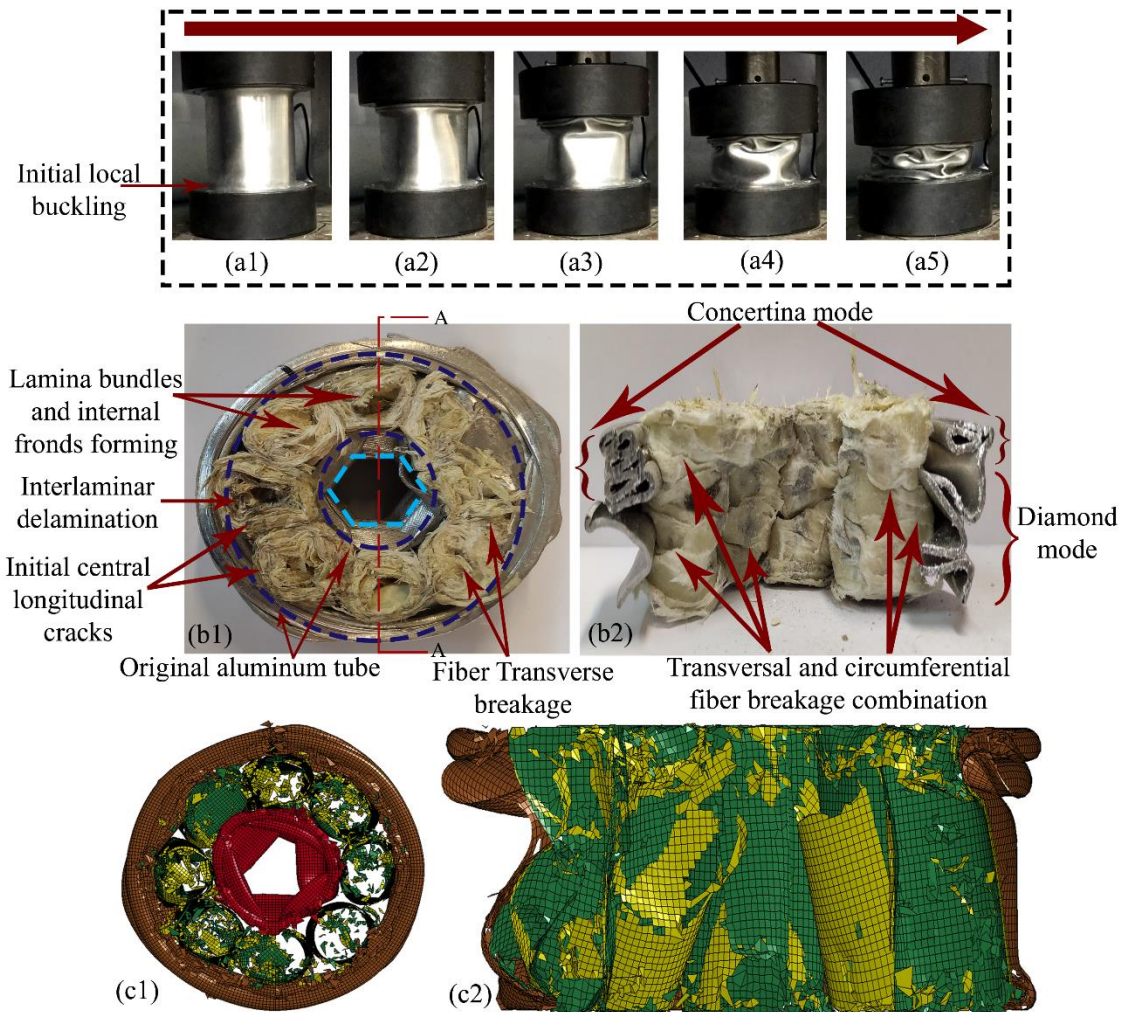


Figure 14: a) sequential images of crushing history of ACA multi-cell tube, b) experimental and c) FEA post crush view of top and cross-section of specimen.

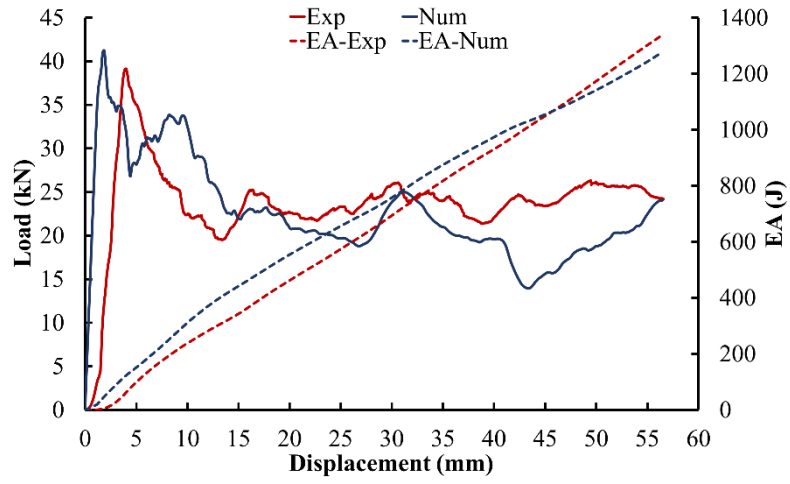


Figure 15: load-displacement and corresponding EA of ACC specimens that were obtained.

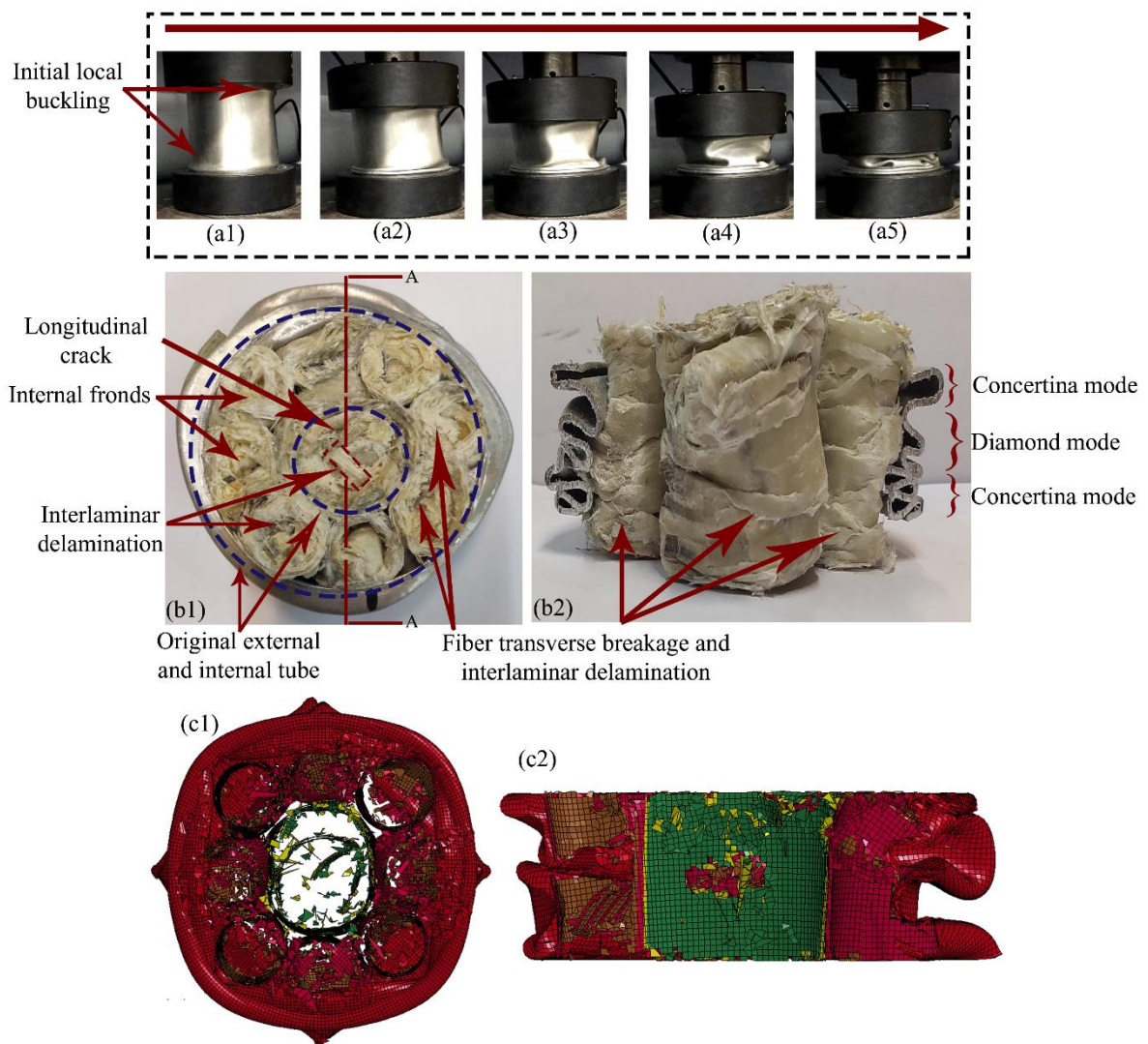


Figure16: a) sequential images of the crushing history of an ACC multi-cell tube: b) experimental and c) FEA post- crush view of the top and cross-section of specimen.

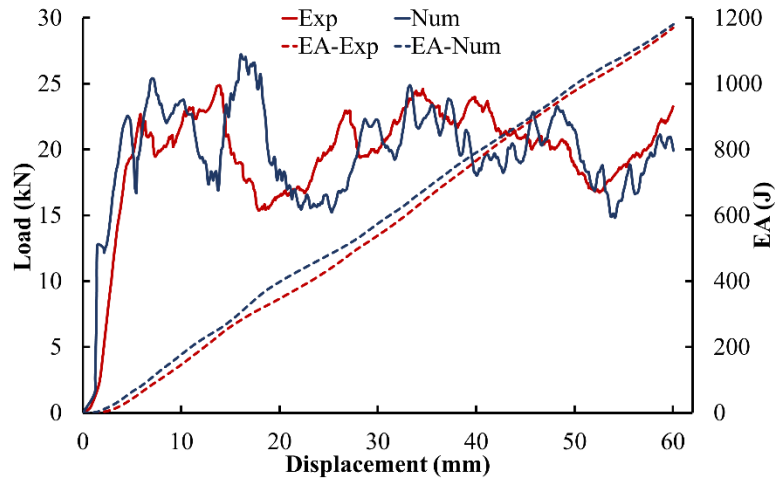


Figure 17: obtained load-displacement and corresponding EA of the CCC specimens.

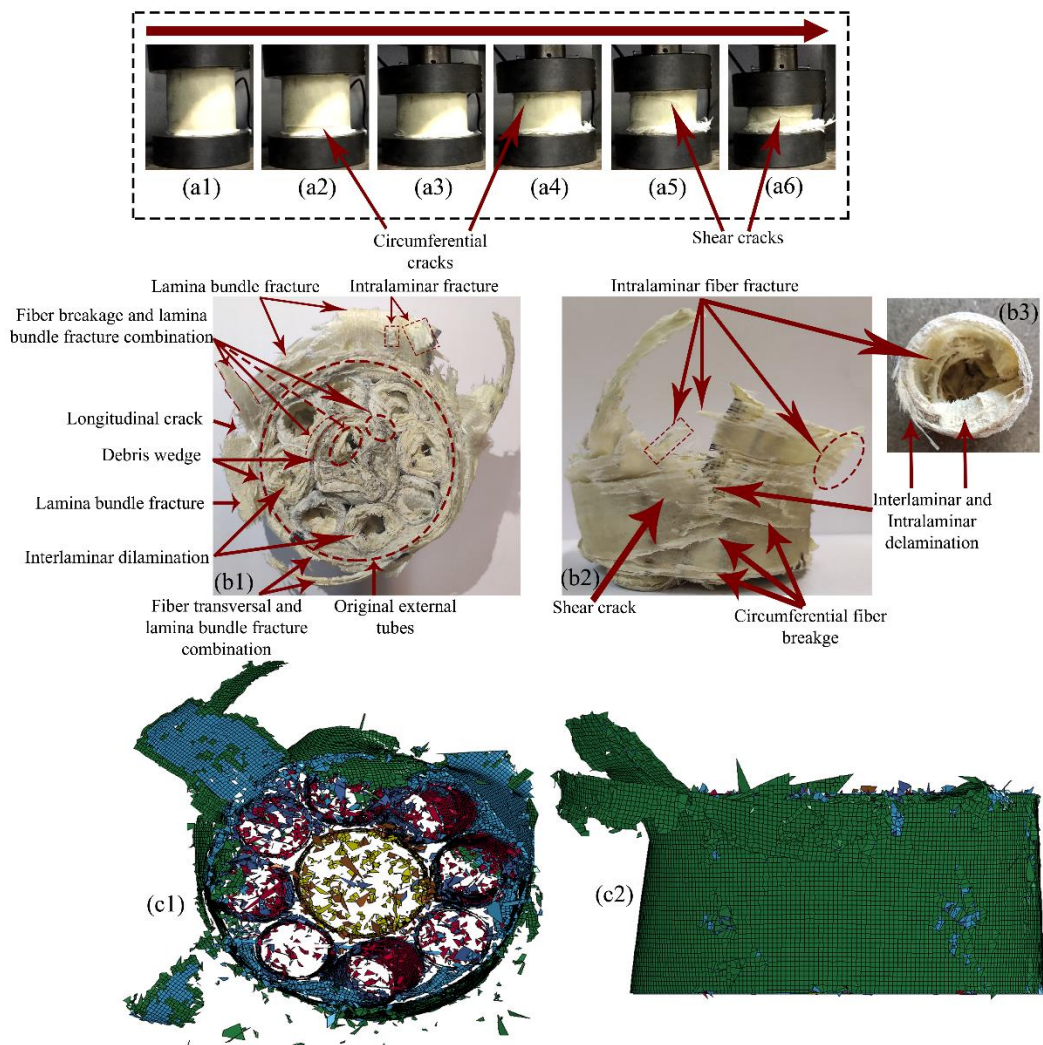


Figure 18: a) sequential images of the crushing history of the CCC multi-cell tube: post crush view of top and side of specimen b) experimental and c) simulation.

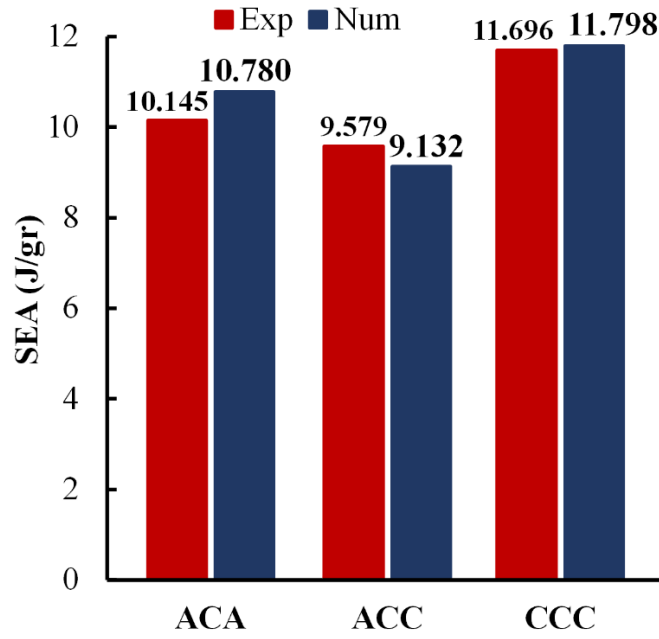


Figure 19: experimental and numerical comparison of SEA of fabricated multi-cell sandwich panels.

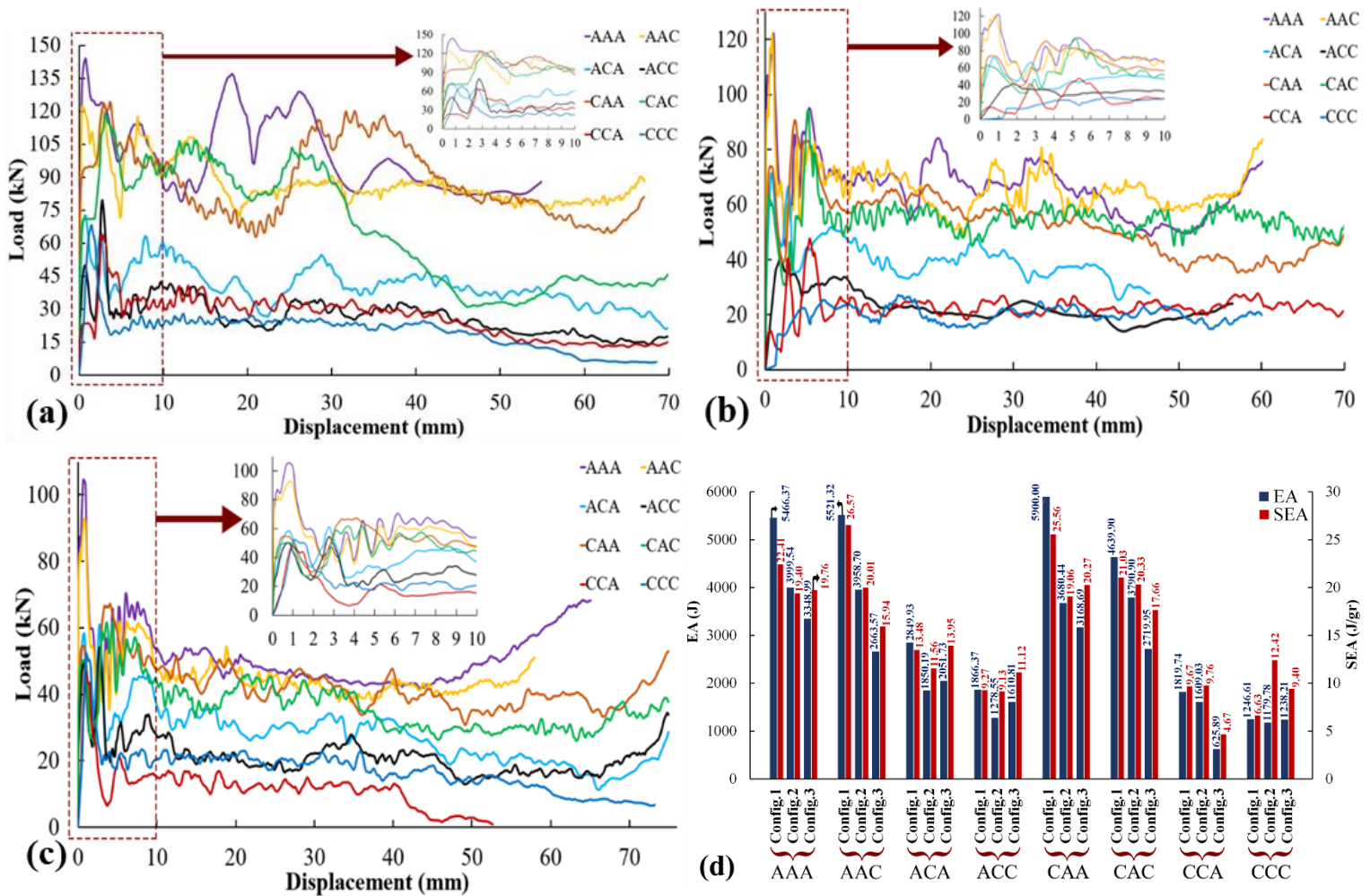


Figure 20: Comparative load-displacement curves of hybrid multi-cell tubes under study: a) config. 1, b) config. 2, c) config. 3 and d) the calculated EA and SEA corresponding to each sandwich tube.

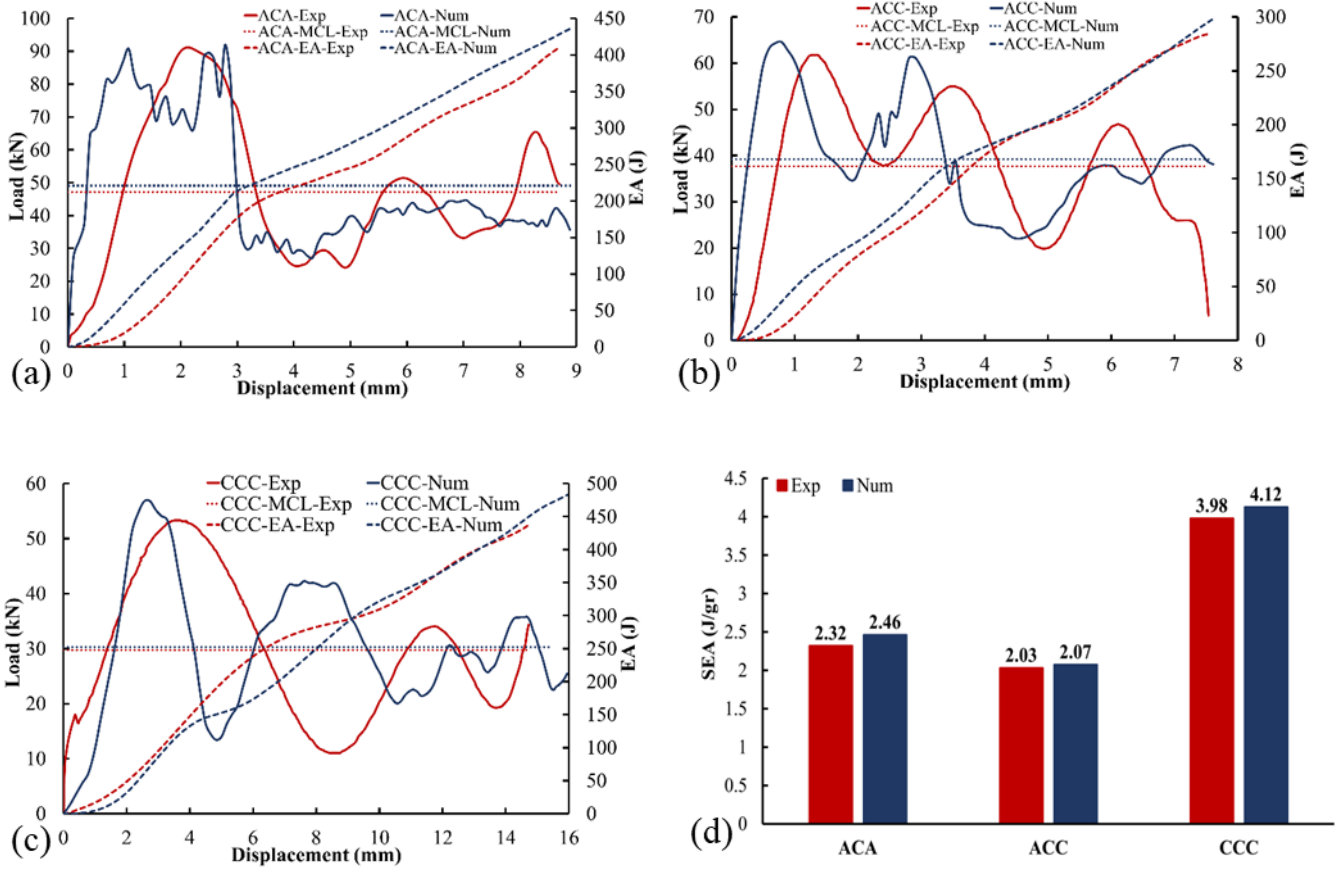


Figure 21: Load-displacement and energy-displacement of (a) ACA, (b)ACC, and c) CCC and d) corresponding SEA values

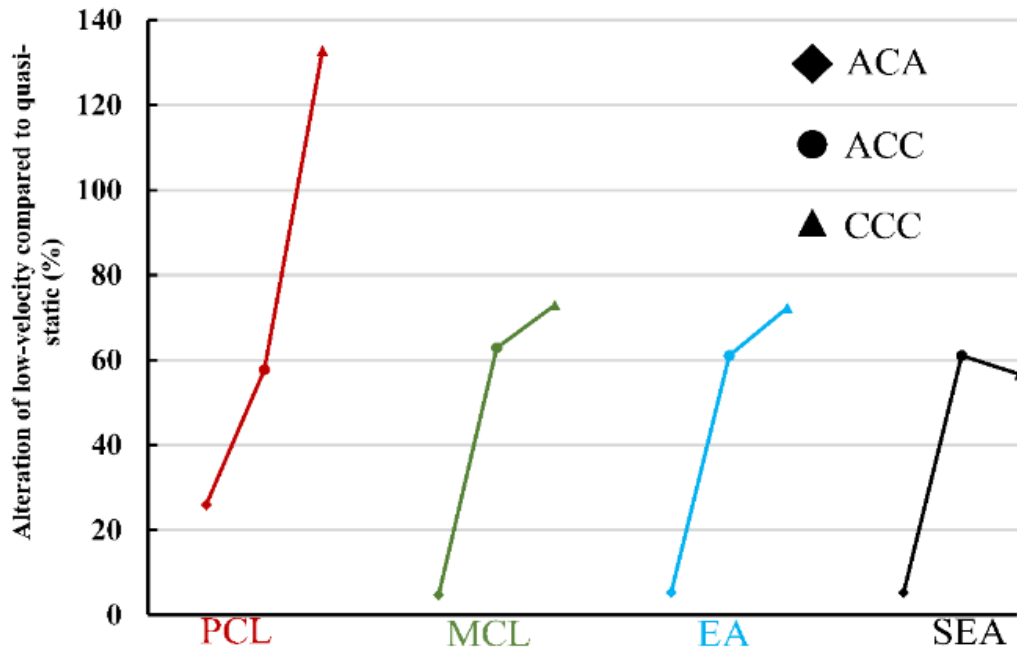


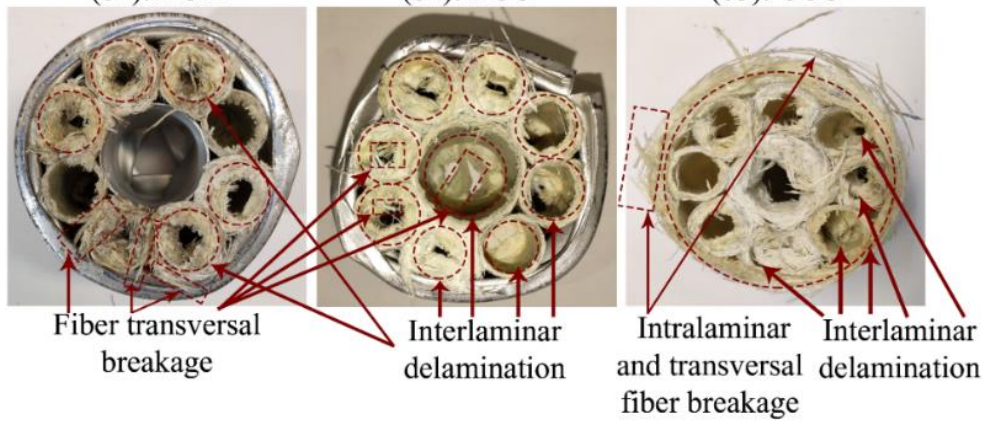
Figure 22: Variations of crush parameters in low velocity compared to quasi-static conditions.



(b1): ACA

(b2): ACC

(b3): CCC



(C1): ACA

(C2): ACC

(C3): CCC



Figure 23: Status of low velocity compression of experiments and simulation.

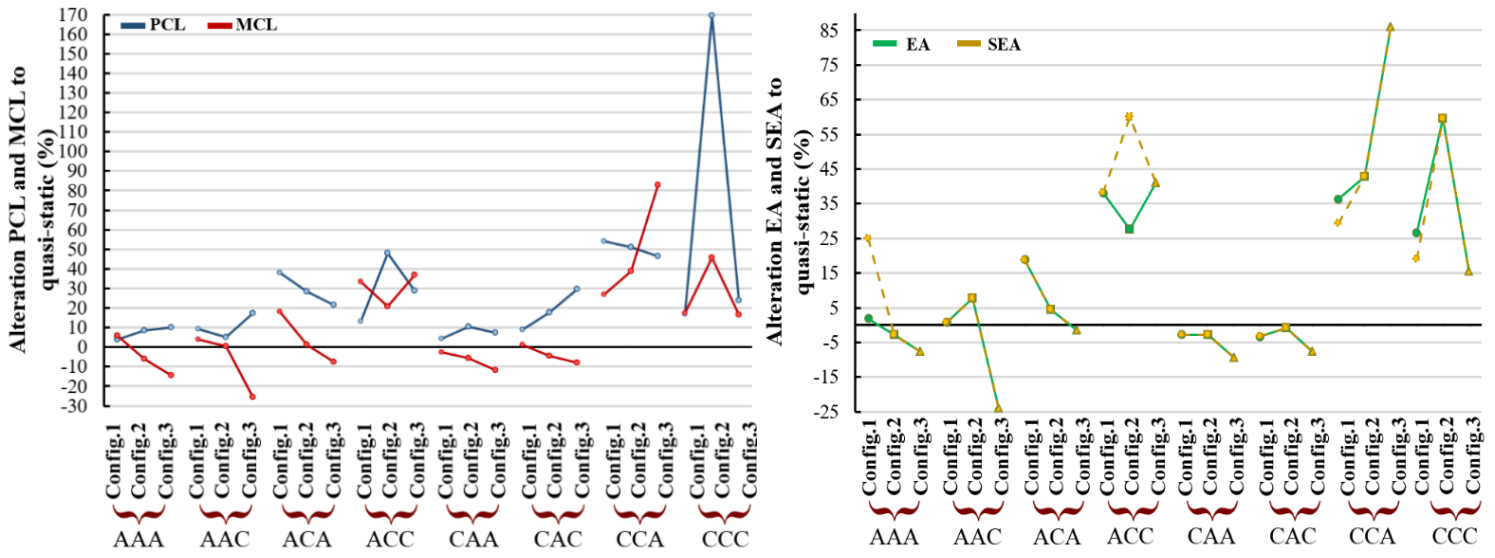


Figure 24: Comparison of low velocity to quasi-static variations of crush parameters.

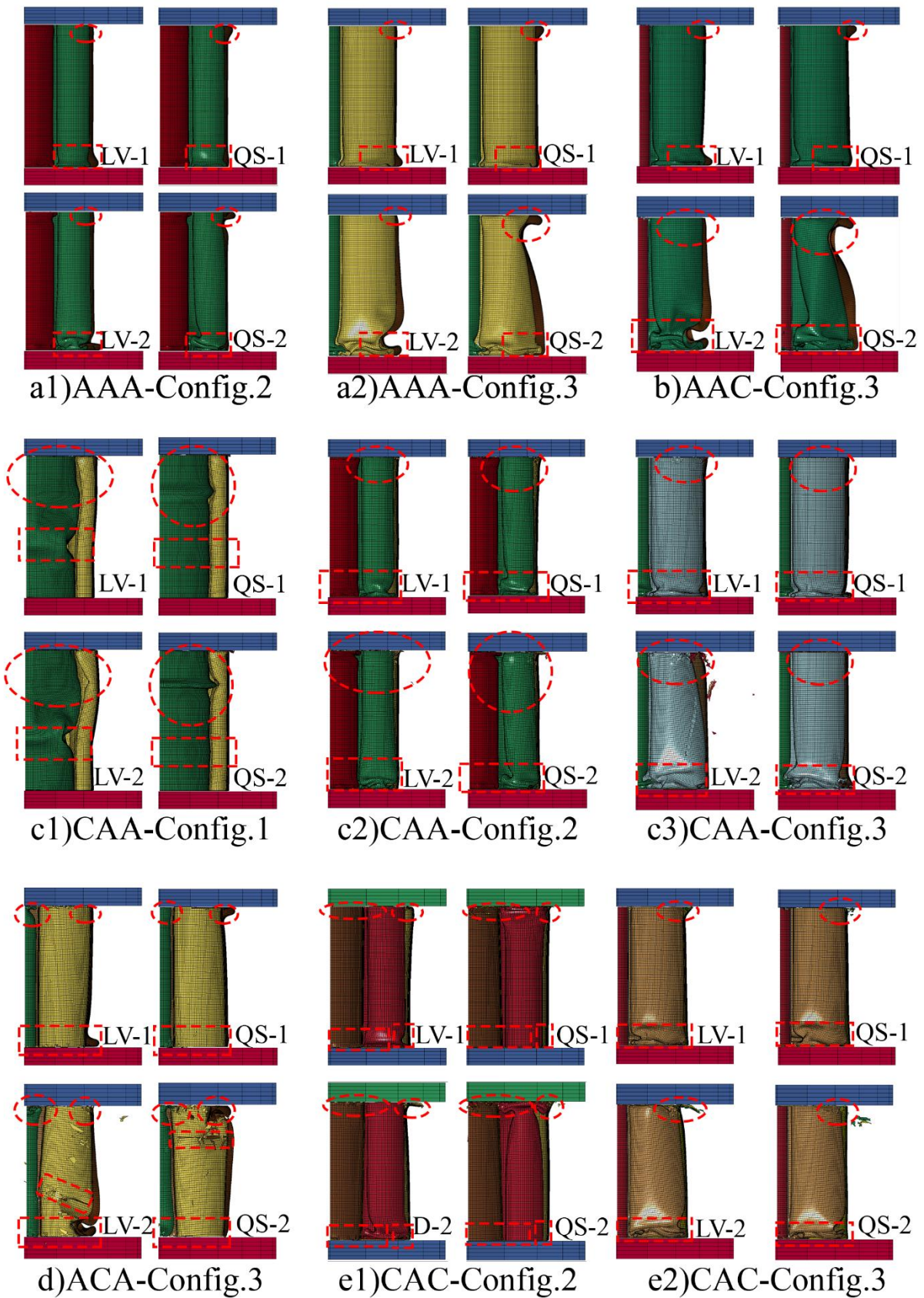


Figure 25: Comparison of crushing mode corresponding to low-velocity (LV) and quasi-static (QS) axial compression. a) AAA, b) AAC, c) CAA, d) ACA, and e) CAC.

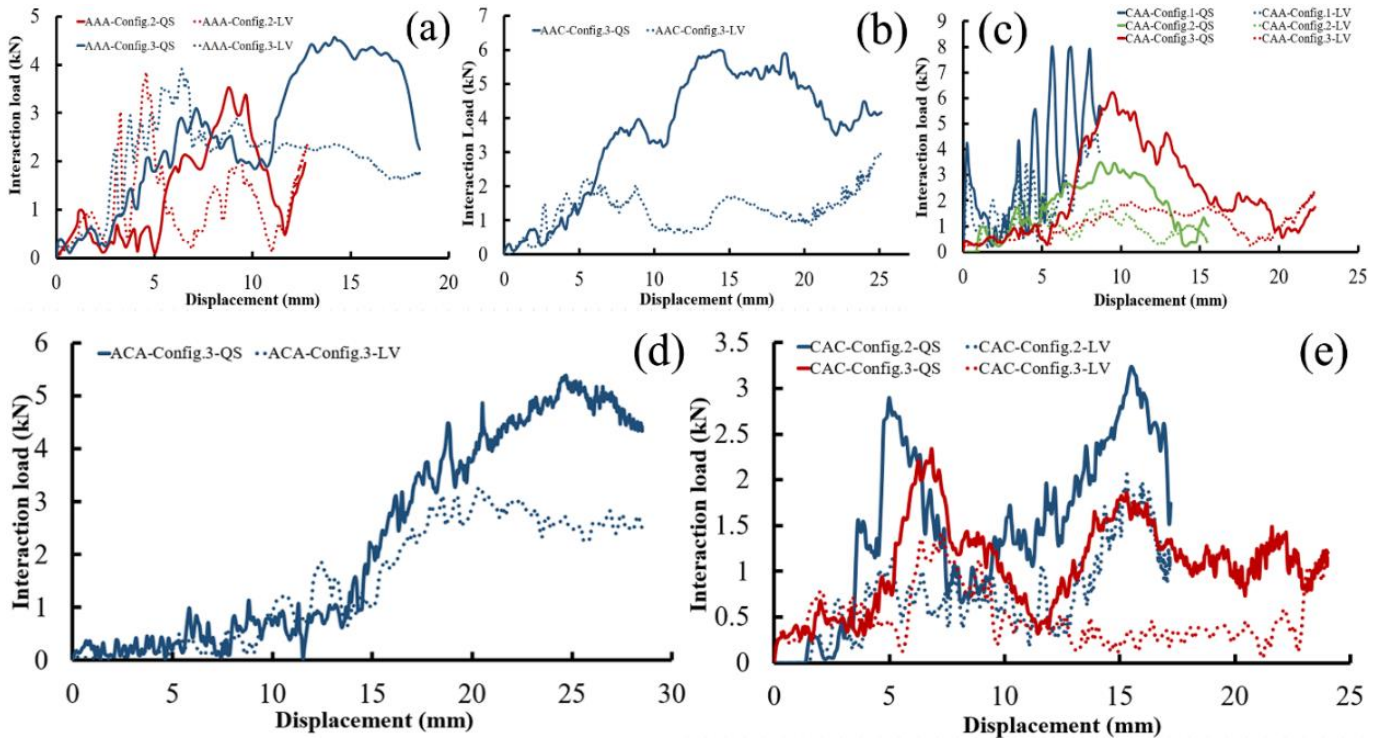


Figure 26: Comparison of interaction loads corresponding to low-velocity (LV) and quasi-static (QS) axial compression. a) AAA, b) AAC, c) CAA, d) ACA, and e) CAC.

**Tables:**



	$D_{\text{internal}} = 35 \text{ mm}$
Config. 3	$D_{\text{core}} = 33 \text{ mm}$
	$D_{\text{internal}} = 14 \text{ mm}$

**Table 7**

Summary of the corresponding crashworthiness parameters of the various sandwich configurations.

Material permutation	Configuration	PCL (kN)	MCL (kN)	CLE (%)	Ste (%)
AAA	Config.1	144	99.51	69.10	60.89
	Config.2	123.2	66.47	53.95	66.74
	Config.3	104.4	51.44	49.27	72.24
AAC	Config.1	120	86.94	72.45	74.58
	Config.2	121.62	65.87	54.16	66.74
	Config.3	92.8	45.87	49.43	72.22
ACA	Config.1	72.45	40.55	55.97	77.91
	Config.2	71.13	39.72	55.84	51.58
	Config.3	60.93	27.34	44.87	83.24
ACC	Config.1	79.6	26.55	33.35	77.91
	Config.2	41.22	22.71	55.09	62.77
	Config.3	54.277	21.47	39.56	83.24
CAA	Config.1	123.6	87.75	71.00	74.58
	Config.2	90.61	52.5	57.94	77.74
	Config.3	66.7	42.23	63.31	83.24
CAC	Config.1	118.9	66.02	55.53	77.91
	Config.2	94.16	54.15	57.51	77.70
	Config.3	61.73	36.24	58.71	83.24
CCA	Config.1	63.59	25.89	40.71	77.91
	Config.2	47.71	22.94	48.08	77.74
	Config.3	47.03	11.85	25.20	58.50
CCC	Config.1	68.37	19.88	29.08	76.17
	Config.2	27.1	20.48	75.57	66.78
	Config.3	52.32	16.88	32.26	79.10

**Table 8**

Calibrated failure strain parameters of E/glass fibers

Woven	DFAILT	DFAILC	DFAILM	UD	DFAILT	DFAILC	DFAILM
	0.15	-0.2	0.16		0.075	-0.95	0.076

**Table 9**

Summary of the corresponding crashworthiness parameters of the various sandwich configurations.

Material permutation	configuration	PCL (kN)	MCL (kN)	EA (J)	SEA (J/gr)	CLE (%)	Ste (%)
AAA	CONFIG1	149.8	119.3	969.45	4.00	79.64	9.29
	CONFIG2	133.6	70.95	971.17	4.71	53.11	14.65
	CONFIG3	114.82	48.51	976.50	5.76	42.25	20.57
AAC	CONFIG1	131.1	104.67	935.66	4.15	79.84	10.06
	CONFIG2	127.73	71.62	973.22	4.92	56.07	14.79
	CONFIG3	108.8	38.54	811.26	4.85	35.42	22.59
ACA	CONFIG1	100	59.89	952.98	4.51	59.89	17.42
	CONFIG2	92.1	48.38	429.23	2.40	52.53	9.68
	CONFIG3	74	31.63	954.73	6.49	42.74	31.29
ACC	CONFIG1	90	45.07	975.13	4.84	50.08	23.00
	CONFIG2	61	38.77	300.00	2.03	63.56	8.44
	CONFIG3	70	33.07	977.37	6.75	47.24	31.89
CAA	CONFIG1	128.7	98.9	860.72	3.73	76.85	9.67
	CONFIG2	100.08	60.41	973.92	5.04	60.36	16.80
	CONFIG3	71.5	42.37	976.17	6.24	59.26	24.69
CAC	CONFIG1	129.53	91.05	965.87	4.38	70.29	11.44
	CONFIG2	110.8	53.05	976.62	5.24	47.88	19.08
	CONFIG3	80	39.5	976.86	6.34	49.38	26.56
CCA	CONFIG1	98	42.77	974.76	4.91	43.64	23.42
	CONFIG2	72	31.99	943.17	5.72	44.43	28.70
	CONFIG3	68.8	26.78	958.31	7.15	38.92	39.09
CCC	CONFIG1	79.94	30.25	909.67	4.54	37.84	32.01
	CONFIG2	56.84	29.94	482.57	4.12	52.67	17.56
	CONFIG3	64.8	24.37	970.40	7.37	37.61	42.11

# Tables:

**Table 1**

Mechanical properties of a Woven[44]and UD glass/epoxy composite

Woven		UD	
Property	value	property	value
Density(kg/m <sup>3</sup> )	1400	Density(kg/m <sup>3</sup> )	1890
Fiber volume fractions (%)	42	Fiber volume fractions (%)	49
Young's moduli, E <sub>1</sub> , E <sub>2</sub> , E <sub>3</sub> (GPa)	19.99, 19.99, 4.76	Young's moduli, E <sub>1</sub> , E <sub>2</sub> , E <sub>3</sub> (GPa)	39, 15, 15
Poisson's ratios, $\nu_{12}$ , $\nu_{13}$ , $\nu_{23}$	0.17	Poisson's ratios, $\nu_{12}$ , $\nu_{13}$ , $\nu_{23}$	0.24
Shear moduli, G <sub>12</sub> , G <sub>13</sub> , G <sub>23</sub> (GPa)	1.49, 1.68, 1.68	shear moduli, G <sub>12</sub> , G <sub>13</sub> , G <sub>23</sub> (GPa)	1.49
Tensile strengths, X <sub>1</sub> , X <sub>2</sub> (MPa)	295.45, 295.45	tensile strengths, X <sub>1</sub> , X <sub>2</sub> (MPa)	1190, 73
Compressive strengths, Y <sub>1</sub> , Y <sub>2</sub> (MPa)	149.4, 149.4	compressive strengths, Y <sub>1</sub> , Y <sub>2</sub> (MPa)	1001, 159
Shear strengths, S <sub>12</sub> (MPa)	91	shear strengths, S <sub>12</sub> (MPa)	36

**Table 2**

Failure parameters for the material model defined for the glass fiber composite.

Parameter	description	woven	UD
DFAILT	tensile strain failure in fiber direction	0.033	0.028
DFAILC	compressive strain failure perpendicular to fiber direction	0.05	0.03
DFAILM	tensile or compressive strain failure for matrix	0.034	0.029

**Table 3**

Comparison between the experimental and numerical crush parameters of ACA.

Crashworthiness parameters	Experimental	Numerical	Relative error (%)
PCI (kN)	70.23	71.67	2.05
MCL (kN)	38.8	39.85	2.70
EA (J)	1808.85	1850.19	2.45
CLE (%)	55.24	55.60	0.64

**Table 4**

Comparison between the experimental and numerical crush indicators of ACC

Crashworthiness parameters	Experimental	Numerical	Relative error (%)
PCI (kN)	39.15	41.22	5.28
MCL (kN)	23.69	23.63	0.25
EA (J)	1341.05	1278.60	4.65
CLE (%)	60.51	57.49	6.29

**Table 5**

Comparison between experimental and numerical crush indicators of CCC.

Crashworthiness parameters	Experimental	Numerical	Relative error (%)
PCI (kN)	22.20	21.10	4.95
MCL (kN)	19.49	20.48	5.07
EA (J)	1169.06	1179.80	0.91
CLE (%)	86.19	97.06	12.61

**Table 6**

Parametric study identification

Geometry characteristics		Material permutation							
Config. 1	$\begin{cases} D_{\text{core}} = 10 \text{ mm} \\ D_{\text{internal}} = 60 \text{ mm} \end{cases}$	AAA	AAC	ACA	ACC	CAA	CAC	CCA	CCC
Config. 2	$\begin{cases} D_{\text{core}} = 20.4 \text{ mm} \\ D_{\text{internal}} = 35 \text{ mm} \end{cases}$								
Config. 3	$\begin{cases} D_{\text{core}} = 33 \text{ mm} \\ D_{\text{internal}} = 14 \text{ mm} \end{cases}$								

**Table 7**

Summary of the corresponding crashworthiness parameters of the various sandwich configurations.

Material permutation	Configuration	PCL (kN)	MCL (kN)	CLE (%)	Ste (%)
AAA	Config.1	144	99.51	69.10	60.89
	Config.2	123.2	66.47	53.95	66.74
	Config.3	104.4	51.44	49.27	72.24
AAC	Config.1	120	86.94	72.45	74.58
	Config.2	121.62	65.87	54.16	66.74
	Config.3	92.8	45.87	49.43	72.22
ACA	Config.1	72.45	40.55	55.97	77.91
	Config.2	71.13	39.72	55.84	51.58
	Config.3	60.93	27.34	44.87	83.24
ACC	Config.1	79.6	26.55	33.35	77.91
	Config.2	41.22	22.71	55.09	62.77
	Config.3	54.277	21.47	39.56	83.24
CAA	Config.1	123.6	87.75	71.00	74.58
	Config.2	90.61	52.5	57.94	77.74
	Config.3	66.7	42.23	63.31	83.24
CAC	Config.1	118.9	66.02	55.53	77.91
	Config.2	94.16	54.15	57.51	77.70
	Config.3	61.73	36.24	58.71	83.24
CCA	Config.1	63.59	25.89	40.71	77.91
	Config.2	47.71	22.94	48.08	77.74
	Config.3	47.03	11.85	25.20	58.50
CCC	Config.1	68.37	19.88	29.08	76.17
	Config.2	27.1	20.48	75.57	66.78
	Config.3	52.32	16.88	32.26	79.10

**Table 8**

Calibrated failure strain parameters of E/glass fibers

Woven	DFAILT	DFAILC	DFAILM	UD	DFAILT	DFAILC	DFAILM
	0.15	-0.2	0.16		0.075	-0.95	0.076

**Table 9**

Summary of the corresponding crashworthiness parameters of the various sandwich configurations.

Material permutation	configuration	PCL (kN)	MCL (kN)	EA (J)	SEA (J/gr)	CLE (%)	Ste (%)
AAA	CONFIG1	149.8	119.3	969.45	4.00	79.64	9.29
	CONFIG2	133.6	70.95	971.17	4.71	53.11	14.65
	CONFIG3	114.82	48.51	976.50	5.76	42.25	20.57
AAC	CONFIG1	131.1	104.67	935.66	4.15	79.84	10.06
	CONFIG2	127.73	71.62	973.22	4.92	56.07	14.79
	CONFIG3	108.8	38.54	811.26	4.85	35.42	22.59
ACA	CONFIG1	100	59.89	952.98	4.51	59.89	17.42
	CONFIG2	92.1	48.38	429.23	2.40	52.53	9.68
	CONFIG3	74	31.63	954.73	6.49	42.74	31.29
ACC	CONFIG1	90	45.07	975.13	4.84	50.08	23.00
	CONFIG2	61	38.77	300.00	2.03	63.56	8.44
	CONFIG3	70	33.07	977.37	6.75	47.24	31.89
CAA	CONFIG1	128.7	98.9	860.72	3.73	76.85	9.67
	CONFIG2	100.08	60.41	973.92	5.04	60.36	16.80
	CONFIG3	71.5	42.37	976.17	6.24	59.26	24.69
CAC	CONFIG1	129.53	91.05	965.87	4.38	70.29	11.44
	CONFIG2	110.8	53.05	976.62	5.24	47.88	19.08
	CONFIG3	80	39.5	976.86	6.34	49.38	26.56
CCA	CONFIG1	98	42.77	974.76	4.91	43.64	23.42
	CONFIG2	72	31.99	943.17	5.72	44.43	28.70
	CONFIG3	68.8	26.78	958.31	7.15	38.92	39.09
CCC	CONFIG1	79.94	30.25	909.67	4.54	37.84	32.01
	CONFIG2	56.84	29.94	482.57	4.12	52.67	17.56
	CONFIG3	64.8	24.37	970.40	7.37	37.61	42.11